Breast Cancer Research

RESEARCH

Open Access

Divergent paths of mammary gland involution: unveiling the cellular dynamics in abruptly and gradually involuted mouse models

Sarmila Majumder[1*†], Sanjay Mishra[2†], Neelam Shinde[1†], Maria C. Cuitino[3], Morgan Bauer[1], Dinesh Ahirwar[2], Mustafa M. Basree[1], Vijaya Bharti[2], Kate Ormiston[1], Resham Mawalkar[1], Sara Alsammerai[1], Gautam Sarathy[1], Anna E. Vilgelm[2], Xiaoli Zhang[4], Ramesh K. Ganju[2] and Bhuvaneswari Ramaswamy[1*^]

Abstract

Background Epidemiological studies associate an increase in breast cancer risk, particularly triple-negative breast cancer (TNBC), with lack of breastfeeding. This is more prevalent in African American women, with significantly lower rate of breastfeeding compared to Caucasian women. Prolonged breastfeeding leads to gradual involution (GI), whereas short-term or lack of breastfeeding leads to abrupt involution (AI) of the breast. Our previous study utilizing a murine model demonstrated precancerous changes, specifically hyperplasia, a non-obligate precursor of breast cancer in the mammary glands of AI mice. Here we investigated mechanisms during early events of AI that prompts precancerous changes in mouse mammary glands.

Methods Uniparous FVB/N mice were randomized to AI and GI on postpartum day 7 when all pups were removed from AI dams. GI dams were allowed to nurse the pups till day 31. Cell death kinetics and gene expression were assessed by TUNEL assay and qPCR respectively. Immune cell changes were investigated by flow cytometry, cytokine array and multiplex immunofluorescence. 3D-organoid cultures were used for in vitro assay of luminal progenitor cells.

Results AI results in rapid cell death, DNA repair response, and immunosuppressive myeloid cells infiltration, leading to a chronically inflamed microenvironment. GI elicits a more controlled immune response and extended cell death. At the peak of cell death, AI glands harbored more immunosuppressive myeloid-derived suppressor cells (MDSCs) and CD206 + M2-like macrophages, known to promote oncogenic events, compared to GI glands. AI glands exhibit an enrichment of CCL9-producing MDSCs and CD206 + M2-like macrophages that promote expansion of ELF5 + /ERα- luminal cells, both in vitro and in vivo. Multiplex imaging of AI glands demonstrated an increase in ELF5 + /WNT5a + luminal cells alongside a reduction in the ELF5 + /ERα + population when involution appeared histologically

Deceased: Bhuvaneswari Ramaswamy.

†Sarmila Majumder, Sanjay Mishra and Neelam Shinde have contributed equally to this work.

*Correspondence:
Sarmila Majumder
sarmila.majumder@osumc.edu
Bhuvaneswari Ramaswamy
Bhuvaneswari.ramaswamy@osumc.edu
Full list of author information is available at the end of the article

complete. A significantly higher number of CD206 + cells in post involution AI gland attests to a chronically inflamed state induced by AI.

Conclusions Our findings reveal significant disparities between AI and GI gland dynamics at the early phase of involution. CCL9, secreted by immune cells at the peak of cell death promotes expansion of Elf5 + /ERα- luminal progenitor cells, the putative precursors of TNBC connecting early events of AI with increased breast cancer risk.

Keywords Breastfeeding, Abrupt involution, Breast cancer, CCL9, M2-like macrophages

Introduction

Epidemiological studies have identified higher parity and lack of breastfeeding as key reproductive factors impacting breast cancer risk, especially triple-negative breast cancer (TNBC) [1, 2]. This is especially relevant in the context of racial disparity in breast cancer outcomes. African American (AA) women have a higher risk of developing TNBC at a younger age, have ~ 40% higher mortality from breast cancer [3], and have a lower prevalence of breastfeeding when compared to Caucasian women (CW) [4].

During pregnancy, the mammary gland undergoes alveologenesis regulated by progesterone and prolactin [5]. At the peak of pregnancy, most of the adipose tissue in the gland is replaced by alveolar cells with some secretory activity, preparing for milk production at partum. Lactation begins with suckling alongside changes in serum estrogen, prolactin, and oxytocin [5]. Weaning of the infant from the mother's milk leads to milk stagnation, which initiates involution, remodeling the glands to a near pre-pregnancy state. The process of involution has been documented to be biphasic, which has been ascertained through mouse models where the forced weaning of pups at the height of lactation induced involution [6]. An initial reversible phase is associated with apoptosis, alveolar cell detachment, and shedding into the lumen for 48 h. This is followed by an irreversible phase when alveolar collapse, a breakdown of the extracellular matrix, the second wave of apoptosis, and massive tissue remodeling occur [6]. These processes lead to the return of the postpartum glands to a near pre-pregnant state histologically with distinguishing features at the molecular level [7, 8]. The key gap in our knowledge is how involution following prolonged breastfeeding and gradual weaning differs mechanistically from abrupt weaning following a lack of or short-term breastfeeding. This is critical to understand as multiple epidemiological studies have described a reduced breast cancer risk following prolonged breastfeeding (> 6 months *vs.* < 3 months) [1, 9–12]. These data imply a significant mechanistic difference between involution following short-term *vs.* long-term breastfeeding.

Indeed, our recent studies in FVB/N mice documented precancerous changes including hyperplasia, metaplasia, increased collagen deposition, and chronic inflammatory changes in abruptly involuted (AI) mammary glands, monitored over 4 months following forced weaning [13]. Our lab noted similar observations in C57BL/6 mice (*unpublished data*). None of these changes were observed in gradually involuting dams allowed to nurse for 28–31 days postpartum (PPM), thus providing valuable insight into the mechanism of protective effects of prolonged breastfeeding against breast tumorigenesis.

Given the observed long-term changes induced by AI *vs.* GI, specifically hyperplasia, a non-obligate precursor of breast cancer and chronic inflammation, our current study sought to understand early events of involution in both groups, starting on day 7 PPM. While AI is induced by the removal of all pups from the dam on day 7 PPM, the pups of the GI mice were allowed to wean naturally until day 28 PPM when lactation and involution occur in parallel. Using a comprehensive approach, we evaluated the histological changes, gene expression patterns, and involvement of myeloid cells during the involution process. Our data demonstrates a stark difference in the early events of AI *vs.* GI with respect to acute phase response, immune microenvironment, and DNA damage response. AI glands displayed a distinct pattern of myeloid cell infiltration, with the predominance of M2-like CCL9 + macrophages, compared to GI glands. Multiplex high-dimensional immunofluorescence revealed an abundance of CD206 + /CCL9 + macrophages in the AI glands at the peak of cell death and that CCL9 promoted the expansion of estrogen receptor-α negative (ERα -) luminal progenitor cells. These cells were previously shown to be the putative precursors of TNBC [14]. These distinct early changes in AI glands could explain the hyperplasia reported in our previous study [13]. The physiological significance of these mechanistic differences and the immune microenvironment could explain the epidemiological link between the length of breastfeeding and breast cancer risk.

Methods and materials

Mouse model

Mice experiments were performed in accordance with a protocol approved by The Ohio State University, University Laboratory Animal Resources, and Institutional

Animals Care and Use Committee. FVB/N mice (Jackson Laboratories, USA, strain# 001800) were maintained in-house in barrier cages, under aseptic conditions, and provided with chow diet (Teklad, Envigo) and water ad libitum. Eight-week-old virgin mice were paired with males and housed individually once pregnant. Only uniparous mice were used in all our studies. Within 24 h of partum, litter size was standardized to 6 pups/dam. Mice were randomized to GI and AI cohorts at 7 days PPM when all 6 pups were removed from the dams of the AI cohort. For the GI cohort, gradual weaning was achieved by the removal of 3 pups each on PPM days 28 and 31. Mammary glands were harvested from the dams on PPM days 7, 8.5, 10, 11, 12, 17, 22, 25, and 28. All experimental animals were humanely euthanized by CO_2 inhalation followed by cervical dislocation before necropsy.

RNA isolation and microarray analysis

RNA was isolated from snap-frozen mammary glands or sorted luminal progenitor cells [13] using Trizol reagent (Invitrogen, USA), subjected to DNase digestion and quality checked using Nanodrop RNA 6000 nanoassays and Bioanalyzer. Gene expression analysis was performed at the Microarray Shared Resource Facility, at The Ohio State University Comprehensive Cancer Center (OSUCCC) using the Affymetrix GeneChip® Mouse Transcriptome Array 1.0 platform (Affymetrix Inc, Santa Clara, CA). Transcriptomic Analysis Console software (TAC, Thermo Fisher Scientific) was used to analyze the gene expression data, where genes with twofold change in expression and a p value < 0.05 were considered significantly altered between the two groups. The gene expression data was subjected to Gene Set Enrichment Analysis (GSEA) (http://software.broadinstitute.org/gsea/msigdb/index.jsp) querying the C2 curated, hallmark 34 gene sets, within the Molecular Signatures Database (MSigDB). Pathways with FDR q-value ≤ 0.25 and p-value ≤ 0.05 were considered for further investigation.

qRT-PCR analysis

The right inguinal gland from each mouse (n = 3 mice per group per time point) after removal of the lymph node was snap-frozen. Frozen mammary glands were disrupted in Trizol (Invitrogen, USA) using a mechanical disruptor (Precellys 24 Touch, Bertin Technologies, USA) and total RNA was isolated using Norgen total RNA isolation kit (Norgen Biotek Corporation, USA). In-column DNase digestion was performed to remove genomic DNA contamination. cDNA was synthesized from DNase-treated RNA using a cDNA synthesis kit (Applied Biosystems, USA). qRT-PCR analysis was performed in triplicates using a StepOne Real-Time PCR machine (Applied Biosystems, USA). RPL37 was used as a housekeeping gene. Primer sequences are provided in Supplementary Table S1.

Western blot analysis

Whole tissue extracts were prepared from snap-frozen mammary glands in RIPA buffer (50 mM Tris–HCL,150 mM NaCl, 0.1% SDS, 0.05% Na-deoxycholate, 1% NP-40) using a tissue disruptor (Precllys, Bertin Technologies, France). Thirty micrograms of protein separated by SDS-PAGE routinely were probed with specific antibodies. Primary antibodies used included anti-CD14 (Cell Signaling Technology, CST # 93882), anti-cathepsin B (CST#31718), anti-BCL-xL (CST#2764), anti-BCL-xS (PA5-32203, Invitrogen), anti-Cleaved PARP (CST#9548), and β-actin (CST#3700). Images were captured by LI-COR imaging system or on X-ray film using electrochemiluminescence based imaging system.

Immunohistochemistry (IHC) and Immunofluorescence (IF)

Freshly harvested mammary glands were fixed in a 10% neutral-buffered formalin solution for 72 h and stored in 70% ethanol. Formalin-fixed, paraffin-embedded (FFPE) sections stained with Haematoxylin and Eosin (H&E) were used for histological analysis, conducted by a board-certified veterinary pathologist. Immunostaining of the FFPE sections was performed in-house with primary antibodies, followed by the detection of bound antibodies using HRP-conjugated or fluorescent-conjugated secondary antibodies as described earlier [13, 15]. Primary antibodies used for IHC and IF were anti-pStat3^{Y705} (1:100, #9145, Cell Signaling Technology, USA), CD14 (1:50, #60253–1, Invitrogen, USA) and anti-F4/80 (1:500, MF48000, Invitrogen, USA).

TUNEL staining

FFPE sections (4 μm) of mammary glands were subjected to TUNEL staining using the TUNEL Assay Kit, (Abcam, USA). Stained slides were imaged using Vectra 3.0 and analyzed using InForm software. One thoracic mammary gland from each mouse (n = 6 mice per group per time point) was used for the analysis. A minimum of twenty high-power images captured by Vectra 3.0 microscope were selected randomly for analysis.

Adipocyte quantification

Mammary gland sections were stained with F4/80 (Cell Signaling Technology #70076) by IHC. Images of stained tissue sections containing at least 50% area composed of adipocytes were captured at 20 × magnification using EVOS Microscope (ThermoFisher Inc). Five images from each mammary gland section were quantified manually using ImageJ software. Only structurally intact adipocytes were quantified. Crown-like structures (CLS) were

identified and quantified by two independent researchers. CLS were identified as any adipocyte surrounded at least 50% by macrophages positive for F4/80 stain.

Flow cytometry and cell sorting

Mammary glands were harvested and chopped into fine pieces using a tissue chopper (McIlwain Tissue Chopper, USA), followed by digestion with 1X collagenase/hyaluronidase mixture in 5 mL of DMEM media supplemented with 10% FBS for 1 h at 37 °C. The enzymes were neutralized by adding 9 mL of DMEM media with 10% FBS and filtered through a 70 µm cell strainer. The single-cell suspensions were centrifuged at 350Xg for 4 min at 4 °C. The cell pellets were suspended in 1 mL of RBC lysis solution (Gibco, USA) and incubated at 37 °C for 10 min. This was followed by adding of 10 mL phosphate buffer saline (PBS) and centrifuged at 350Xg for 5 min at 4 °C. The cell pellets were suspended in Fc blocking buffer as per the manufacturer's instructions (BioLegend, San Diego, CA). The cells were washed and incubated with a cocktail of fluorophore-conjugated antibodies specific to different populations of inflammatory cells and Zombie Aqua live/dead dye for 30 min on ice. Single-color controls were prepared in parallel. The cells were washed twice with PBS, the samples were acquired on Cytek Northern Lights-3000, and the data was analyzed using FlowJo software. For cell sorting, single-cell suspensions of mammary glands stained with different antibodies as described above were processed on BD flow activated cell sorter Aria III to collect CD11b + /F4/80 + / CD206 + populations.

Cytokine profiling

The sorted cell population was subjected to cytokine array analysis (Ray Biotech, USA) as per the manufacturer's instructions. Briefly, an equal number of cells from each group were lysed using cell lysis buffer. The array membranes were incubated for 30 min in a blocking buffer followed by incubation with the cell lysates at 4 °C overnight. The membranes were next washed and incubated with a biotinylated secondary antibody cocktail, washed again, and incubated with HRP-Streptavidin solution for 2 h at room temperature. Membranes were then washed and exposed to X-ray film. The films were scanned to obtain digital images and analyzed for expression intensity using ImageJ software (NIH, USA). The expression intensity density was normalized to internal control after subtracting the background.

Luminal Progenitor (LP) organoid culture

LP cells were cultured as organoids in vitro following a protocol by Vilgelm *et. al* [16]. Briefly, the sorted LP cell suspension from 6-weeks old virgin female mice (FVB/N) was washed with 1X Hank's Balanced Salt Solution (HBSS). 10,000–40,000 cells were mixed with 100 µL Cultrex Basement Membrane Extract (BME) and plated in pre-warmed low attachment spheroid microplates (96 wells). The plate was incubated at 37 °C for 1 h and supplemented with complete DMEM medium (advanced supplemented with 10% FBS and antibiotics), N-acetylcysteine (1.25 mM), Nicotinamide (10 mM), N-2 Supplement (1X), B-27 Supplement (1X), Y-27632 dihydrochloride (10 µM), hEGF (10 ng/mL), hFGF-10 (10 ng/mL), hFGF-2 (1 ng/mL), Hydrocortisone (0.3 µg/mL), Insulin (1 µg/mL), β-estradiol (0.5 nM), R-spondin (100 ng/mL), Noggin (100 ng/mL) and Heregulin (5 nM). The organoids were passaged every 10–12 days using TrypLE™ (Gibco) or Trypsin to break down the organoids into smaller clusters of cells and re-plating them (10,000 cells in each well) in BME domes as described above. For treatment, PBS or CCL9 (100 ng/mL) was added twice a week in a supplemented medium and organoids number, as well as morphology, were monitored regularly using a bright field microscope, and the number of branching in organoids was counted as described in our earlier study [17].

Multiplex immunofluorescence (mIF) study

For simultaneous antibody detection on FFPE mammary gland tissue sections, mIF was carried out utilizing the Opal fluorophore coupled to tyramide signal amplification (TSA) system from Akoya Biosciences (Marlborough, MA, USA). As part of the panel development process, staining conditions were first adjusted using serial tissue sections that underwent tests for antibody stripping and pH- and temperature-dependent antigen retrieval. To determine the optimal mIF conditions, Opal-antibody pairings were evaluated based on marker abundance and co-expression within cellular compartments to limit the possibility of spectral crosstalk. For example, high-expressing biomarkers were coupled with less intense Opals, and *vice versa*, to facilitate spectral acquisition. To assist mIF optimization, the InFORM® software (Akoya Biosciences, version 2.4.11) was utilized to evaluate biomarker signal-to-background ratio (signal: noise ≥ 10:1) and signal balance (signal intensity of adjacent Opals ≤ 10:1) into other channels.

The optimized mIF staining workflow consisted of antigen retrieval by incubating tissue sections in ER2 solution (pH 9, 100 °C; Leica Biosystems, Vista, CA, USA) for 30 min using the Leica Bond RX autostainer. According to the Panel Chart, the first primary antibody (CCL9) was incubated for 30 min, followed by anti-mouse/rabbit-HRP conjugate labeling and Opal-TSA polymer incubation for 10 min. The stripping phase consisted of either ER1 (pH 6, Leica Biosystems) or ER2 solutions incubated

at 95–98 °C for 20 min between each antibody staining round. After staining with the second antibody (CCR1), the protocol was repeated until all the markers were applied. The tissue sections were then counterstained for 5 min with spectral DAPI, rinsed with TBS, and mounted with ProLong® Diamond Antifade Mountant (Life Technology, Carlsbad, CA, USA).

Panel chart

Order	Antibodies	Dilutions	Opal Fluorophores	Opal Dilution	Stripping (pH/min/°C)
1	CCL9	1:100	480	1:150	6/20/95
2	CCR1	1:100	570	1:150	6/20/98
3	ERα	1:100	620	1:150	9/20/95
4	WNT5a	1:100	690	1:150	6/20/95
5	ELF5	1:50	520	1:150	6/20/95
6	CD206	1:200	780	1:25	6/20/95

The Phenoimager HT multispectral digital slide imaging system (Akoya Biosciences) was used to capture whole-slide scans. The mammary gland tissue images were scanned at desired magnification and 0.5 µm/pixel resolution, with each region of interest (ROI) measuring 931 µm × 698 µm. The entire slide scans were opened in Phenochart (Akoya Biosciences) for manual ROI annotation. The margins of tissues were excluded due to the possibility of staining artifacts. InFORM® was used to access the annotated ROIs for additional image processing, such as spectral unmixing and autofluorescence correction. Anti-CD20 antibody was paired with each Opal fluorophore (without DAPI counterstain) as a single plex to create a spectral library for spectral correction yielding a single component image. After unmixing, InFORM® was utilized to generate machine-learning algorithms for cell segmentation and binary phenotyping using a set of component images. This included instructing inFORM® to distinguish individual cells stratified by inclusion within tissue regions, and by cell morphology and marker expression patterns to classify cells into positive or "other" categories. The intensity of each marker (e.g., normalized counts/exposure time per cytoplasm, membrane, and/or nucleus) was utilized to compute the thresholds for marker positivity. For example, DAPI and ELF5 labeling allowed nuclei to be detected based on intensity and size, while CCR1 staining aided in delineating membrane structures to refine borders relative to adjacent cells. After optimizing the segmentation and phenotyping algorithm on a small subset of ROIs, the semi-optimized algorithm was used in batch analysis on the remaining ROIs. All ROIs were evaluated for agreement with machine learning, and those that did not pass, such as harboring false positives due to fluorescence from nearby cells, were retrained yielding the optimized algorithm. Finally, the InFORM® data was merged and quantified using the R programming language in phenoptrReports (version 0.3.2, Akoya Biosciences). The cell density for each cell type was estimated for each selected image as the number of positive cells per area (cell counts/mm^2) and then normalized to the total nucleated cells. The average normalized cell percentage and standard error of all randomly selected images for a specific sample were calculated to reflect population and heterogeneity.

Imaging quantification and scoring of chromogenic stains

Images of immune-stained tissue sections from multiple mice were captured using Vectra 3.0 and analyzed using InForm® software. Twenty random fields per tissue section were subjected to blinded quantification. For F4/80, entire images of tissue sections were analyzed. A positive signal threshold for each staining parameter was established prior to quantification. For quantification of phospho-Stat3(Y705), the percentage of DAB-positive cells in the epithelium and stroma were assessed. For F4/80, the total percent of the positive area was used for quantification.

Statistical analysis

Mean ± SD of the quantitative outcomes are shown on the figures. Two sample or paired t-test was used for two group comparisons depending on whether the data is independent or correlated. Linear mixed effects models were used to compare the outcomes with repeated measurements over time to take account of correlations among observations from the same subject. Microarray data was analyzed using Transcriptome Analysis Console (TAC 4.0), and pathway enrichment with the differentially expressed genes was analyzed with the GSEA tool. Holm's procedure was used to adjust for multiple comparisons. An adjusted p value < 0.05 was considered as significance. The SAS 9.4 and R programs were used for data analysis.

Results

Distinct histomorphological features of mouse mammary gland at early stages of gradual *vs*. abrupt involution

To study and compare sequential events during the early stage of GI and AI, we used a mouse model where wild-type females of FVB/N background at 8 weeks of age were set up for breeding. Following partum, litter size was standardized to 6 per dam [13]. Uniparous dams were randomly assigned to GI and AI cohorts. All 6 pups were removed from the AI dams on day 7 PPM. For GI dams, 3 pups each were removed on days 28 and 31

PPM, allowing for prolonged lactation. Multiple studies in the past analyzed early events (0–72 h post-involution) of involution specifically in the AI setting [18–20]. This study focused on mammary glands harvested intermittently between days 8.5 and 28 PPM from mice in both AI and GI cohorts (Fig. 1A). Lactating glands harvested on day 7 PPM (before removal of pups) were used as a baseline. Histological features of sequential stages of mammary gland involution undergoing AI *vs.* GI are captured in Fig. 1B.

Analysis of H&E-stained sections revealed that between days 8.5 and 12 PPM, GI glands were fully lactating and composed of numerous, densely packed, large acini lined by tall cuboidal epithelium and filled with amphophilic secretions, with almost no intervening adipose tissue (Fig. 1B and C). On day 17 PPM, the epithelium lining acini appeared less tall multifocally, and small groups of adipocytes were often present between acini (Fig. 1C). On day 22 PPM, acini were lined by low cuboidal to flattened epithelium, and nuclear debris became apparent in acinar lumens in the form of apoptotic bodies, suggesting acinar breakdown (Fig. 1C). Larger groups of adipocytes were present between acini (Fig. 1C, adipocytes quantified in Fig. 1E). By day 25, there was a significant increase in adipocyte repopulation, and few intact acini remained (Fig. 1C). In addition, a mixed inflammatory cell population was present multifocally surrounding partly incomplete acinar profiles and admixed with proteinaceous fluid and fat globules (Fig. 1C).

AI glands on day 8.5 PPM (1.5 days after pup removal) were also fully lactating with little intervening adipose tissue. However, acini were lined by flattened epithelium and there was abundant cytoplasmic and karyorrhectic debris admixed with few inflammatory cells indicating prominent acinar breakdown (Fig. 1B and D). On day 11 PPM, the glandular remodeling was more advanced with rare intact acinar profiles, increased numbers of inflammatory cells, and more abundant intervening adipose tissue (Fig. 1B and D). On day 12 PPM, there was a striking reduction of glandular parenchyma, with a significant increase in the area occupied by adipose tissue. Acinar breakdown and inflammatory cells were less prominent than on day 11 (Fig. 1B and D). These changes resembled those observed in GI-day 25 glands. On day 17 PPM, adipose tissue predominated largely in the AI glands and only ducts with a few acini were visible (Fig. 1B and D). The AI glands continued to remodel beyond day 17 and histologically resembled near a pre-pregnant state by day 28 PPM. On the contrary, the GI glands remodeled through day 31 and attained near pre-pregnant histology by day 35 PPM (Supplementary Fig. S1A). Signs of proliferative changes are apparent in day 31 and day35 AI glands that led to hyperplasia as reported earlier [13].

Quantification of adipocyte repopulation showed that in AI glands, repopulation spans over 10-days (day 12 to day 22 PPM), with a sharp increase in adipocyte repopulation in GI glands starting on day 25 and reaching a plateau on day 28 PPM, indicating complete remodeling of the gland (Fig. 1E). This repopulation was associated with simultaneous loss of mammary epithelial cells in both glands (Supplementary Fig. S1B). AI-day 28 glands exhibited a small but significant increase in adipocyte number compared to GI-day 28 glands (Fig. 1F). However, when categorized by size, there was no significant difference in the distribution of adipocytes between AI and GI glands on day 28 PPM (Fig. 1G), along with total adipocyte area, average size, and the number of crown-like structures (Supplementary Figs. S1C, S1D & S1E).

Cell death and DNA damage are more pronounced in AI glands

Apoptotic cells with condensed nuclei started appearing in the lumens of the AI glands as early as day 8.5 PPM, while that was noted on and after day 17 PPM in the GI glands. TUNEL (terminal deoxynucleotidyl transferase dUTP nick end labeling) assay revealed a sharp increase in cell death within 36 h of pup withdrawal (AI-day 8.5 PPM) that peaked on day 11 PPM (5.1 ± 0.02%

(See figure on next page.)

Fig. 1 Histological analysis of mammary glands undergoing gradual *vs*. abrupt involution. **A.** Schematic diagram showing the workflow of mice subjected to abrupt involution (AI) and gradual involution (GI) followed by different harvest times. **B.** Representative images of H&E-stained sections of mouse mammary glands subjected to AI or GI and harvested at different days postpartum (PPM) as indicated. Scale bar = 200 µm **C.** Higher magnification images of H&E-stained section of GI mammary gland on indicated postpartum days. Day 8.5, 11 and 12: black arrows indicate large acini, and clear arrows indicate epithelial cells. Day17: clear arrows indicate epithelial cells, curved black arrows indicate a small group of adipocytes; Day 22: clear arrows indicate flattened epithelial cells, black arrows indicate the nuclear debris and arrowheads indicate repopulating adipocytes. Day 25: arrow heads indicate repopulating adipocytes; black arrows indicate immune cells. **D.** H&E-stained section of AI mammary gland on day 8.5: Grey arrow indicate lactating acini, black arrowheads indicate flattened epithelial cells and black arrows indicate karyorrhectic debris. Day 11: Grey arrows indicate collapsed alveoli, black arrows indicate immune cells and arrowheads indicate adipocytes. Day 12: arrowheads indicate adipose tissues, and black arrows indicate immune cells. Day17: arrow heads indicate adipose tissues. (**C&D:** Scale bar = 100 µm). **E.** Adipocyte repopulation over time, from day 7 to day 35 PPM. n = 6 per group per time point. **F.** Comparison of total number of adipocytes in AI and GI glands harvested on day 28 PPM. **G.** Comparison of total number of adipocytes categorized by size in AI *vs*.GI glands

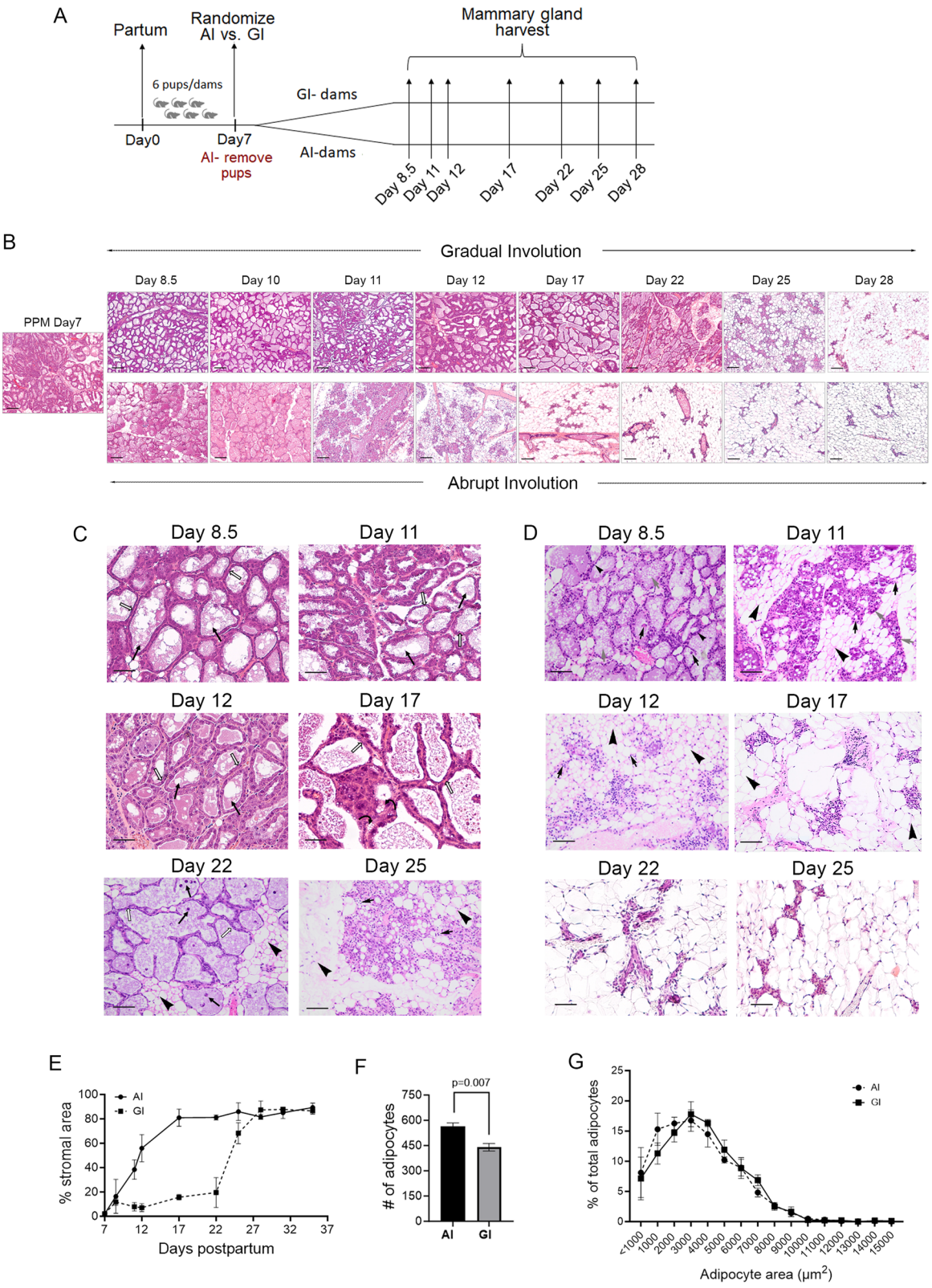

Fig. 1 (See legend on previous page.)

positive cells), followed by an equally sharp decline in cell death and return to near baseline by day 17 PPM (0.42 ± 0.0005% positive cells) (Fig. 2A and B). In contrast, there was a gradual increase in cell death in GI glands after day 12 PPM that peaked on day 25 (3 ± 0.1% positive cells), followed by a gradual decline to baseline by day 31 PPM (0.35 ± 0.0004% positive cells) (Fig. 2A and B). Overall, this shows that AI glands have significantly increased TUNEL-positive cells compared to the GI group averaged across all time points ($p = 0.0005$), predominantly due to the acute increase in cell death in AI glands between days 8.5 and 12.

While we observed a rapid increase in apoptosis in AI glands, the glands also demonstrated an increased activation of the DNA repair pathway. This pathway is one of the Hallmark gene sets [21] that we found differentially enriched in AI-derived LP cells harvested on day 28 PPM (negative enrichment score = 1.74, false discovery rate q-value = 0.0039, p-value = 0.024) when compared to GI-LP cells (Fig. 2C). This suggests an increased DNA damage response in AI glands. To investigate if indeed AI resulted in DNA damage that persisted over time, we analyzed the extent of DNA damage using γH2AX immunohistochemistry (IHC). There was a trend toward higher γH2AX-positive cells in AI *vs.* GI glands at day 120 PPM, although the difference was not statistically significant (Supplementary Fig. S2A, $p = 0.10$). Studies in C57BL/6 mice revealed a similar trend of increased DNA damage in AI-day 120 glands compared to GI-day 120 glands ($p = 0.059$, Fig. 2D and Supplementary Fig. S2B).

In involuting mammary glands, DNA damage initiates checkpoint mechanisms in mammalian cells, leading to cell cycle arrest to facilitate DNA damage repair. If the damage proves insurmountable, cell death is predominantly induced through apoptosis [22, 23]. Therefore, to study the apoptotic response in gradual and abruptly involuting mammary glands, we also analyzed BCL-xL, BCL-xS and the involvement of poly ADP-ribose polymerase (PARP). Levels of BCL-xL in AI glands are high at the onset of involution (day 8.5 PPM) and reduced to a low level (50% of day 7 PPM) on day 12. Although there was a slight increase in BCL-xL between days 17 and 25, surprisingly BCL-xL was very high on day 28 PPM (Figs. 2Ei & Eii). In contrast, we observed a relatively comparable level of BCL-xL at the early time points in GI glands, with the highest expression on day 25 followed by a marked reduction on day 28 (Figs. 2Ei and Eii). On the contrary, BCL-xS was detectable in the AI glands only on day 8.5 PPM. A consistent level of BCL-xS was present till day 22 PPM in the GI glands (Figs. 2Ei & Eiii). This demonstrates that in the AI glands, the key anti-apoptotic response was not as pronounced as in GI glands at the peak of cell death and that BCL-xS supporting mammary epithelial cell survival [24] was higher in both the glands until the onset of involution. Interestingly, the 89 kDa cleaved PARP, a product of caspase-mediated cleavage of PARP, was barely detectable either in the AI or GI glands of the FVB mice (Supplementary Fig. S2C). In contrast, a 55 kDa cleaved PARP, generated by cathepsin B-mediated cleavage [25], was detected in the GI glands; it gradually increased from day 17, peaked at day 25, and remained high on day 28 (Figs. 2Ei & Eiv). In AI glands, we observed a low level of 55 kDa cleaved PARP from day 11 PPM through day 28 PPM when compared to GI glands (Figs. 2Ei, Eiv & Supplementary Fig. S2D). A higher level of 24 kDa cleaved PARP, a trans-dominant inhibitor of PARP [26], was observed at the onset of AI (Figs. 2Ei, Ev & Supplementary Fig. S2D). Similarly, in the GI gland increased 24 kDa cleaved PARP level coincided with peak of cell death that remained high through day 28 PPM, suggesting a sustained inhibition of PARP. Collectively, our findings demonstrate a striking difference in the rate of cell death, adipocyte repopulation, PARP cleavage, and degree of DNA damage between the AI *vs.* GI glands.

Acute phase response genes are expressed primarily during AI but not during GI

The biphasic nature of postpartum mammary gland involution and identification of key players associated with acute phase response (APR) due to massive cell death stemmed from studies in mice subjected to AI following partum and brief lactation (7–10 days) [18, 27, 28]. However, the role of these genes during the gradual involution of mouse mammary glands remains unknown. Therefore, we next attempted to address whether there is a mere shift of key events and heightened expression of the APR genes during the peak of gradual involution

(See figure on next page.)

Fig.2 DNA damage response is heightened in AI glands compared to GI glands. **A.** Representative images of FFPE sections of AI and GI mammary glands subjected to TUNEL assay at indicated time points (day PPM). Arrows indicating apoptotic cells. **B.** Kinetics of cell death between days 7 and 28 PPM, assessed by TUNEL staining. n = 6 per group per time point. **C.** Enrichment plot of HALLMARK_DNA_REPAIR pathway in AI *vs.* GI glands on day 28 PPM. **D.** phospho-γH2AX positivity in, GI and AI glands harvested on day 120 PPM and in mammary glands of age-matched virgin mice. n = 4 per group. **Ei.** Western blot analysis of BCL-xL, BCL-xS and cleaved PARP in AI and GI mammary glands at early phase of involution, quantitated in **Eii.** BCL-xL, **Eiii**. BCL-xS and **Eiv**. 55 kDa cleaved PARP, and **Ev.** 24 kDa cleaved PARP

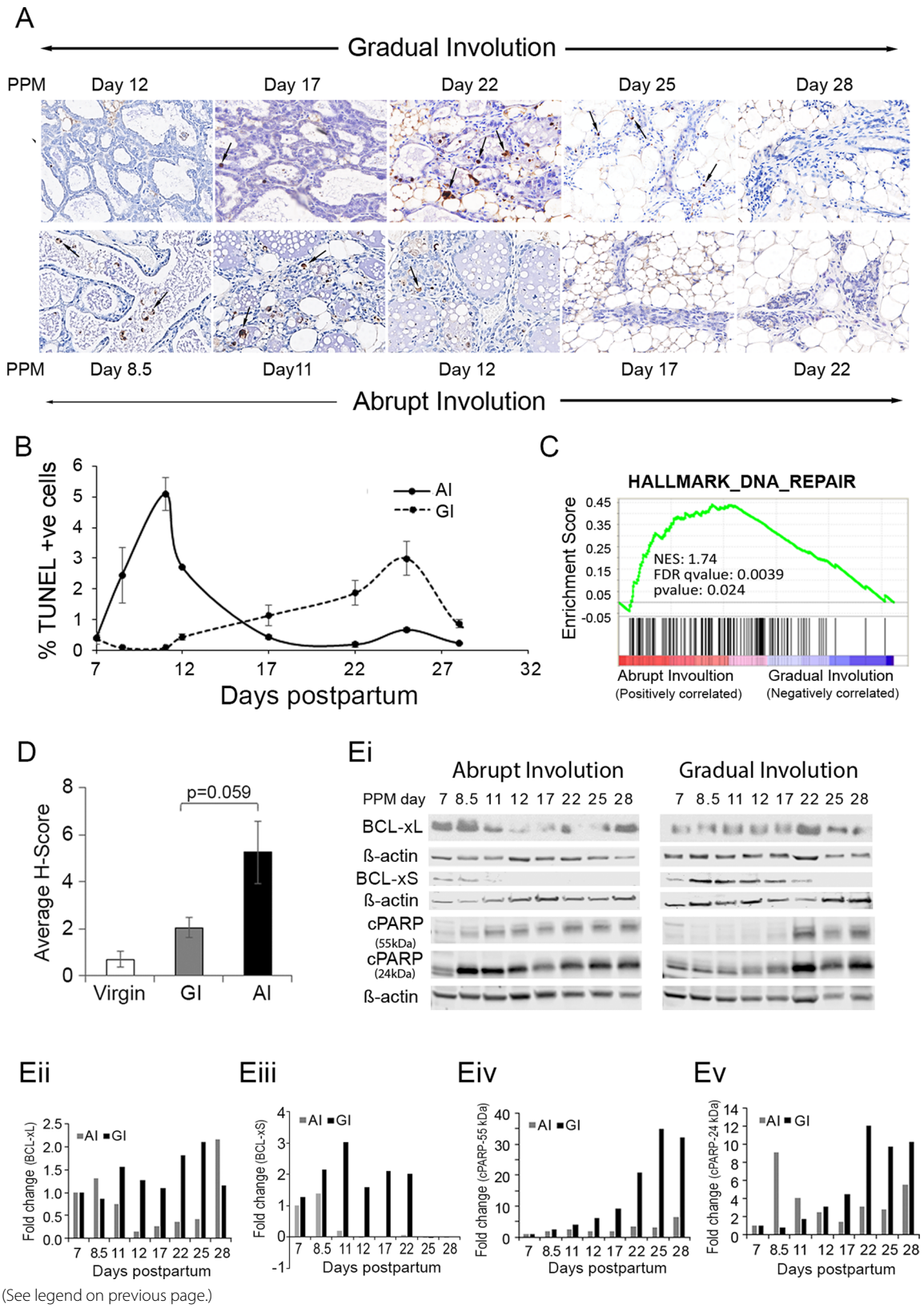

Fig.2 (See legend on previous page.)

(day 17–28 PPM) or alternatively if these changes are less pronounced, thus contributing to the protective effect against breast cancer risk. The fold change for all genes, both RNA and protein levels, at all the time points were measured relative to the levels on day 7 PPM (lactating gland).

In previous studies, STAT3 and C/EBPδ were identified as master regulators of lysosome-mediated program cell death (LM-PCD) [29, 30] using mouse models of AI. In our study, both *Stat3* and *C/ebpδ* expression increased sharply and peaked on day 8.5 PPM (*Stat3*: 5.9-fold, $p=0.0007$, *C/ebpδ*: 4.4-fold, $p=0.008$) in the AI glands, followed by a rapid decline to near baseline by day 12 PPM. In contrast, GI glands showed a gradual increase in *Stat3* expression that peaked on day 22 PPM (4.5-fold, $p=0.06$) followed by a sharp decline on day 25 and thereafter (Figs. 3A and B). *C/ebpδ* expression was barely detectable in the GI glands throughout the process of involution. Western blot analysis demonstrated the highest level of Stat3 protein in the lactating glands that gradually declined with time in both AI and GI glands (Figs. 3Li & Liii). In contrast, the pStat3^{Y705} level in AI glands was highest (15-fold compared to day 7) and comparable at days 8.5 and 12 PPM, followed by a gradual decline until day 25. Interestingly, a second peak (~sevenfold) was observed on day 28 PPM in AI glands. The pStat3^{Y705} level peaked in GI glands on day 22 PPM but was significantly less than that in AI glands at the onset of involution (sevenfold GI-day 22 *vs*. 15-fold AI-day 8.5; Figs. 3Li & Lii). Similarly, a sharp increase in pStat3^{Y705}- positive cells on day 8.5 PPM (0.26% *vs*. 24.8% on days 7 and 8.5, respectively) was observed in the AI glands when mammary gland sections were analyzed by IHC (Supplementary Fig. 3A). This was followed by a 50% drop (11.9%) on day 12 PPM and further declined to 5.6% on day 22 PPM (Fig. 3M). Interestingly, an increase in pStat3^{Y705} positivity was observed on day 25 PPM (8.4%). In GI glands, pStat3^{Y705}-positive cells were undetectable until day 12, followed by a gradual increase to 11.4% positivity on day 25 PPM (Fig. 3M). IHC analysis corroborates the data obtained by qPCR and Western blot analysis in both AI and GI glands.

Analysis of *CtsL* and *CtsB* expression, the two lysosomal cysteine proteases involved in LM-PCD [27], revealed that in the AI glands, there was a sharp induction of *CtsL* (sixfold, $p=0.001$) on day 8.5 PPM followed by a sharp decline on day 11 PPM. *CtsL* expression remained low at the subsequent time points (Fig. 3C). There was no marked change in *CtsL* expression in the GI glands, suggesting a minimal role in cell death during GI (Fig. 3C). Intriguingly, in the AI glands *CtsB* expression showed biphasic expression with the first peak at day 12 PPM (3.5-fold., $p=0.01$), followed by a gradual decline through day 17 and an increase again on day 22 (2.5-fold., $p=0.05$) (Fig. 3D). GI glands did not exhibit this biphasic expression and rather showed a gradual increase over time, which peaked on day 25 (2.6-fold, $p=0.04$) (Fig. 3D). The increased level of *CtsB* expression was concurrent with maximum cell death in the GI glands, suggesting a major role of *CtsB* and not *CtsL* in cell death during GI. We also observed the highest level of CTSB protein (27 kDa) in AI-day 11 glands (~sixfold higher compared to day 7), which started to increase on day 8.5 and decreased after day 12. CTSB protein peaked on day 22 in GI glands (a twofold increase over day 7) and remained elevated through day 28 (Figs. 3Li & Liv, Supplementary Fig. S3B).

Several downstream effectors of Stat3 and predominantly APR/immunomodulatory proteins have been identified to play a key role during mouse mammary gland involution in the AI setting [18]. We analyzed the expression of these key players (*Orm1, Orm2, Lrg1,* and *Slpi*) to assess their role in GI. Both *Orm1* and *Orm2,* the two APR genes, showed a sharp increase in expression in the AI glands following the removal of pups, with the highest expression on day 12 PPM (Orm1: tenfold, $p=0.04$; Orm2: 370-fold, $p=0.05$) and a sharp decline to baseline by day 17 PPM (Fig. 3E and F). In GI glands, *Orm1* expression was highest at day 28 (2.2-fold, $p=0.5$), while *Orm2* was not detectable (Fig. 3E and F). Similarly, expression of *Lrg1*, a late-stage macrophage marker, showed a marked increase on day 12 PPM in AI glands (203-fold, $p=0.01$), followed by a sharp decline to baseline by day 17 PPM and remained low (Fig. 3G). In GI glands, expression of *Lrg1* was undetectable throughout

(See figure on next page.)

Fig.3 Expression pattern of acute phase response genes is distinct in AI and GI glands. Quantitative RT-PCR analysis of **A.** *Stat3*, **B.** *C/EBPδ*, **C.** *CtsL*, **D.** *CtsB*, **E.** *Orm1*, **F.** *Orm2*, **G.** *Lrg1*, **H.** *Slpi*, **I.** *CD14*, **J.** *Chi3L1,* and **K.** *MMP2*. Expression normalized to *RPL37*. n = 3 per group per time point. **Li.** Western blot analysis and quantitation of **Lii.** pStat3^{Y705}, **Liii.** Stat3, **Liv.** CtsB, and **Lv.** CD14. **M.** Temporal pattern of pSTAT3^{Y705} positive cell distribution in AI and GI glands between day 7 and day 28 postpartum. n = 6 per group per time point. **Ni.** Representative images of FFPE sections of AI (day 11 PPM) and GI (day 22 and 25 PPM) mammary glands subjected to immunofluorescence analysis of pStat3^{Y705} (green) and CD14 (red). DAPI (blue) was used to counterstain the nuclei. **Nii.** Bar diagram showing the number of pStat3.^{Y705} and CD14 double-positive cells per field of view (FOV) in mammary gland sections of AI (day 11 PPM) and GI (day 22 and 25 PPM). n = 5 per group per time point. Number of FOV = 10

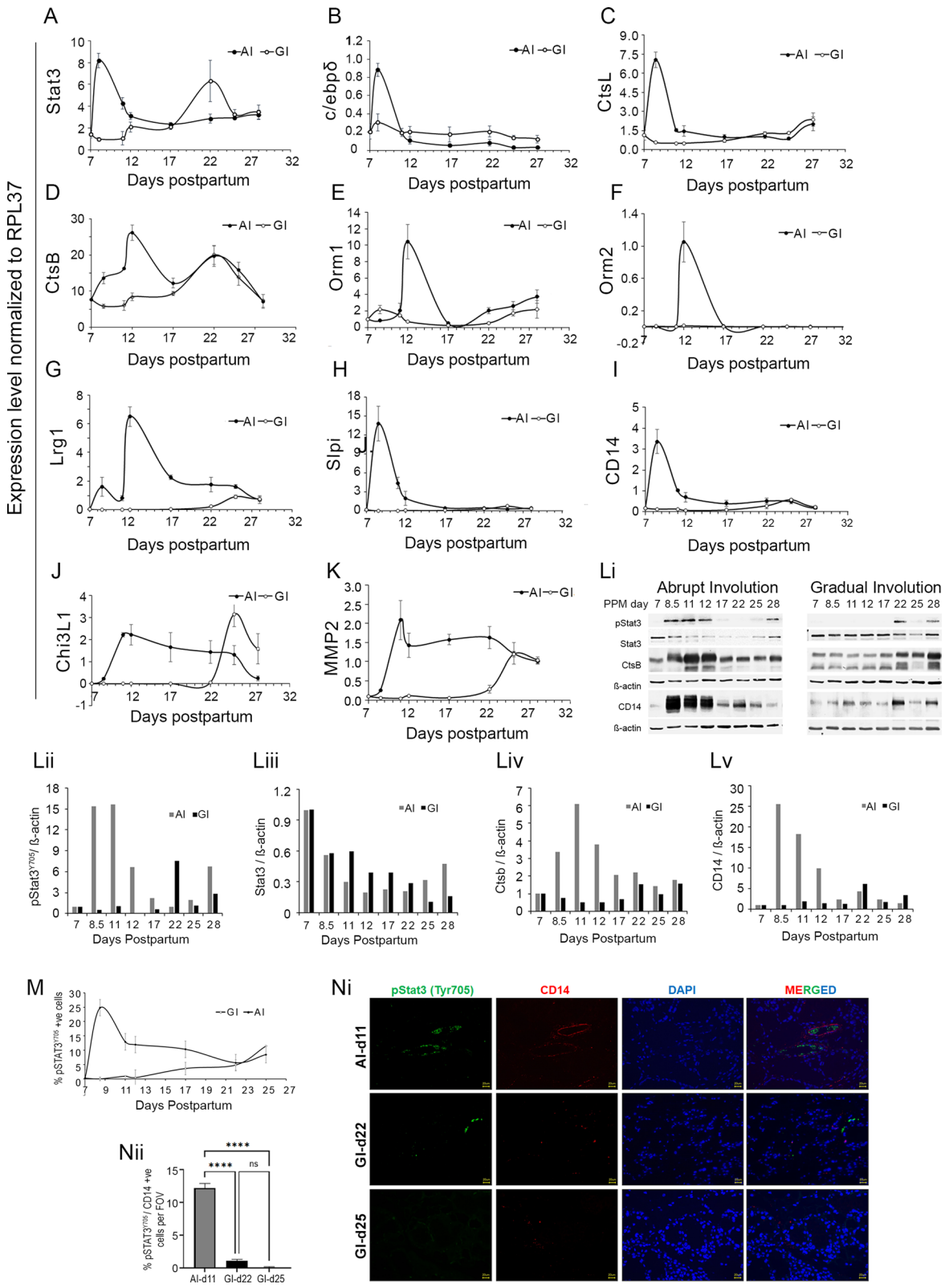

Fig.3 (See legend on previous page.)

with a small increase on day 25 (28-fold, $p=0.02$) (Fig. 3G). Slpi, a secretory leukocyte peptidase inhibitor is an immunomodulatory protein that protects tissue epithelium from serine proteinases [31]. AI glands demonstrated a sharp increase in *Slpi* expression that peaked on day 8.5 PPM (61-fold, $p=0.008$), followed by a decline to baseline by day 12 PPM, whereas its expression was undetectable in GI glands throughout the involution process (Fig. 3H). In brief, these results suggests that while an acute phase response is obvious during AI, GI glands do not display such a response, even at the peak of cell death (day 25 PPM, Fig. 2B).

A key finding by Stein et al. was the significantly high expression of *CD14* by luminal epithelial cells and their potential role in dead cell clearance immediately after the removal of pups in the AI setting [19]. Anticipating a similar role of luminal epithelial cells in GI glands to coincide with maximum cell death, we compared *CD14* expression at both RNA and protein levels between GI and AI glands over time. Our data shows a 20-fold increase in *CD14* expression in the AI glands from day 7 to day 8.5 PPM ($p=0.005$), and a sharp decline by day 11 PPM (Fig. 3I). In contrast, only a very low level of *CD14* expression was observed in the GI glands on day 25 PPM (3.4-fold, $p=0.003$, Figs. 3I). Western blot analysis shows that CD14 protein levels followed a similar pattern as gene expression in both GI and AI glands (Figs. 3Li & Lv, Supplementary Fig. S3C). In the AI glands, the CD14 protein level was highest on day 8.5 PPM (25-fold increase), and in the GI glands, CD14 protein level was highest on day 22 (sixfold increase). We also performed immunofluorescence analysis on AI glands at day 11 PPM and GI glands at days 22 as well as day 25 PPM to assess the presence of alveolar clusters co-expressing phosphorylated Stat3 ($pStat3^{Y705}$) and CD14. Our analysis revealed a significantly higher number of pStat3 + CD14 + cells in the AI glands at day 11 PPM compared to GI glands at days 22 or 25 PPM (Figs. 3Ni & 3Nii, $p<0.001$). Therefore, this data suggests a minimal role of luminal epithelial cells in the clearance of apoptotic cells during GI as opposed to AI.

We next analyzed *Chi3L1* expression, a tissue-restricted marker of late-stage macrophage differentiation involved in wound healing. Increased expression of this gene was reported by Scully et al. during mammary gland involution in the AI setting [32]. Our data shows that *Chi3L1* expression in AI glands peaked on day 11 PPM (555-fold, $p=0.002$) and remained high until day 22, which was followed thereafter by a gradual decline until day 28 (Fig. 3J). In the GI glands, *Chi3L1* gradually increased after day 22 PPM and peaked on day 25 (750-fold, $p=0.03$). Expression of *MMP2*, a matrix metalloprotease involved in the restructuring of post-involution glands [33], was high in AI glands as early as day 11 PPM and remained high until day 22 PPM, while it was upregulated in GI glands around day 25 PPM (Fig. 3K).

Altogether, based on gene and protein expression analysis of the whole mammary glands, we see diverse and distinct patterns between AI and GI glands, which are summarized in Table 1.

Myeloid-derived suppressor cells and M2-like macrophages release CCL9 in AI glands at the peak of cell death

Our previous study demonstrated that inflammation persists in the mammary glands that had undergone AI, whereas it is transient in the GI glands with a quick return to baseline [13]. Here we examined the kinetics of immune cell infiltration at the early stages of AI *vs.* GI, specifically, at the peak of cell death. Analysis of macrophage infiltration by IHC (F4/80) revealed a sharp increase in AI glands following removal of the pups that

Table 1 Expression pattern of acute phase response genes

	Gene	Function related to Involution	References
Up in both AI and GI glands	*Stat3*	Acute phase response protein, lysosome mediated cell death	Kreuzaler et.al. [27]
	CtsB	Lysosome-mediated programmed cell death	Sargeant et.al. [29]
	Chi3L1	Macrophage marker, dead cell clearance	Stein et.al. [19]
	MMP2	Mammary stromal remodeling	Uria et.al. [33]
Up in AI glands only	*C/ebpδ*	Regulator of pro-apoptotic genes	Thangaraju et.al. [30]
	CtsL	Lysosome-mediated programmed cell death	Sargeant et.al. [29]
	Orm1	Acute phase response protein	Clarkson et.al. [28]
	Orm2	Acute phase response protein	Clarkson et.al. [28]
	Lrg1	Neutrophil-granulocyte marker, dead cell clearance	Stein et.al. [19]
	Slpi	Secretory leukocyte inhibitory protein, limits damaging effect of residual neutrophils	Clarkson et.al. [28]
	CD14	Monocyte -macrophage marker, dead cell clearance	Clarkson et.al. [28]

peaked on day 11 PPM (35 ± 8%) and gradually declined to ~ 14% positivity on day 17 PPM. Interestingly, there was a second surge of macrophages (~ 23% positive cells) on days 22 and 25 PPM (Fig. 4A and Supplementary Fig. S4). In contrast, macrophage infiltration in GI glands remained low until day 12 PPM, followed by a slow and gradual increase over time to 27 ± 7% positivity on day 25 PPM. Statistical analysis shows that AI has significantly increased F4/80 staining compared to the GI group averaged across all the time points ($p = 0.0005$) by 6.62%; this was mainly attributed to the differences at the earlier time point (days 11 and 12 PPM). This data demonstrates a biphasic pattern of macrophage infiltration in the AI gland, an acute inflammatory response at the onset of involution, and a second surge later around day 25 PPM. Intriguingly, our previous study demonstrated a decline in F4/80 positive cells in GI glands at later time point (day 56 PPM), while it continued to remain high in the AI glands [13]. Thus, in the GI gland, the macrophage infiltration is more restricted coinciding with cell death and declines once involution is complete while in the AI glands it is sustained beyond cell death.

Next, we assessed the myeloid cell composition during the peak of cell death in both gland types based on previous reports showing the recruitment of various myeloid cell subsets in the developing and inflamed mammary gland [34]. Their relative abundance varies during post-lactational regression and contributes to a microenvironment conducive to tumor growth [35]. However, a comparative analysis of myeloid cell distribution in AI and GI mammary glands has not been conducted so far. Histological examination of H&E-stained sections revealed a significant increase in inflammatory cell infiltration starting on day 11 in AI glands and day 25 in GI glands, coinciding with the respective cell death peaks (Figs. 1 & 2).

To further analyze myeloid cell populations, we performed multi-color flow cytometric analysis on AI-day 11 and GI-day 25 mammary glands. The relative abundances of total CD45 + leukocytes and CD11b + F4/80 + total macrophages were not statistically different between these two groups (Fig. 4B and D). However, we observed a significant enrichment of CD11b + Gr1 + myeloid - derived suppressor cells (MDSCs) in mammary glands from AI-day 11 compared to GI-day 25 (Fig. 4C), while MHCII + M1-like macrophages did not exhibit a significant change between the two groups (Fig. 4E). On the other hand, CD11b + F4/80 + CD206 + cells that were identified as M2-like macrophages (pro-tumor) [36] were more abundant in AI-day 11 compared to GI-day 25 glands (Fig. 4F). To further characterize the functional properties of macrophage subpopulations, Gr1 + MDSCs and CD206 + M2-like macrophages were sorted from AI-day 11 and GI-day 25 glands and subjected to mouse cytokine/chemokine array analysis. Both MDSCs and M2-like macrophages from AI glands showed a significant increase in the expression of CCL9 compared to their counterparts from GI-day 25 mammary glands (Fig. 4G and H). Additionally, qRT-PCR validation demonstrated significantly higher *Ccl9* expression in AI glands, however, showing a biphasic expression (Fig. 4I). Previous studies have shown that TGFβ3 promotes the recruitment of inflammatory cells by upregulating the production of chemokines/cytokines such as CCL9 [37]. Additional studies reported TGFβ3 upregulation and its active involvement during mammary gland involution [38, 39]. To connect the dots, we measured the expression of *Tgfβ1*, *Tgfβ2*, and *Tgfβ3* in GI and AI glands. Importantly, our data shows significantly increased expression of only *Tgfβ3* that coincides with cell death peak in both AI and GI glands (Fig. 4J). In the AI glands, *Tgfβ3* expression is elevated again around day 22 PPM. The marked overlap in the biphasic pattern of *Ccl9* and *Tgfβ3* expression in the AI glands suggests a possible role of TGFβ3 in regulating *Ccl9* expression. Conversely, *Tgfβ1* and *Tgfβ2* expression was undetectable in both AI and GI glands. Taken together, these results show that at the peak of cell death, AI glands have more MDSCs and

(See figure on next page.)

Fig. 4 Abundance of myeloid-derived suppressor cells and M2-like macrophages in AI glands at the peak of cell death secreting CCL9. **A.** Temporal pattern of F4/80 positive cell distribution in AI and GI mammary glands harvested between days 7 and 25 PPM. FFPE sections of mammary glands were subjected to IHC using F4/80 antibody. Images of the stained slides were captured using Vectra 3.0 and analyzed using InForm software. n = 6 per group per time point. **B.** Mammary glands from AI-day 11 and GI-day 25 female mice were processed to identify different subpopulations of myeloid cells by multi-color flow cytometry. The representative flow cytometric dot plots and graphs of % **B.** CD45 + leukocytes; **C.** CD11b + Gr1 + MDSCs (out of CD45 + cells); **D.** CD11b + F4/80 + total macrophages (out of CD45 + cells); **E.** MHCII + M1-like macrophages (out of CD45 + CD11b + F4/80 + total macrophages); **F.** CD206 + M2-like macrophages (out of CD45 + CD11b + F4/80 + total macrophages); n = 3 per group. **G.** CD11b + Gr1 + MDSCs, and H. CD11b + F4/80 + MHCII-CD206 + M2-like macrophages were sorted from mammary glands of AI-day 11 and GI-day 25 mice. The cells were lysed and subjected to cytokine/chemokine array analysis. The images show expression of cytokine/chemokine and bar diagrams showing CCL9 expression quantified using ImageJ software. **I.** Quantitative RT-PCR analysis of *Ccl9* expression in mammary glands over time (days 7 to 28 PPM), n = 3 per group. **J.** Quantitative RT-PCR analysis of *Tgfβ3*expression in mammary glands over time (days 7 to 28 PPM), n = 3 per group

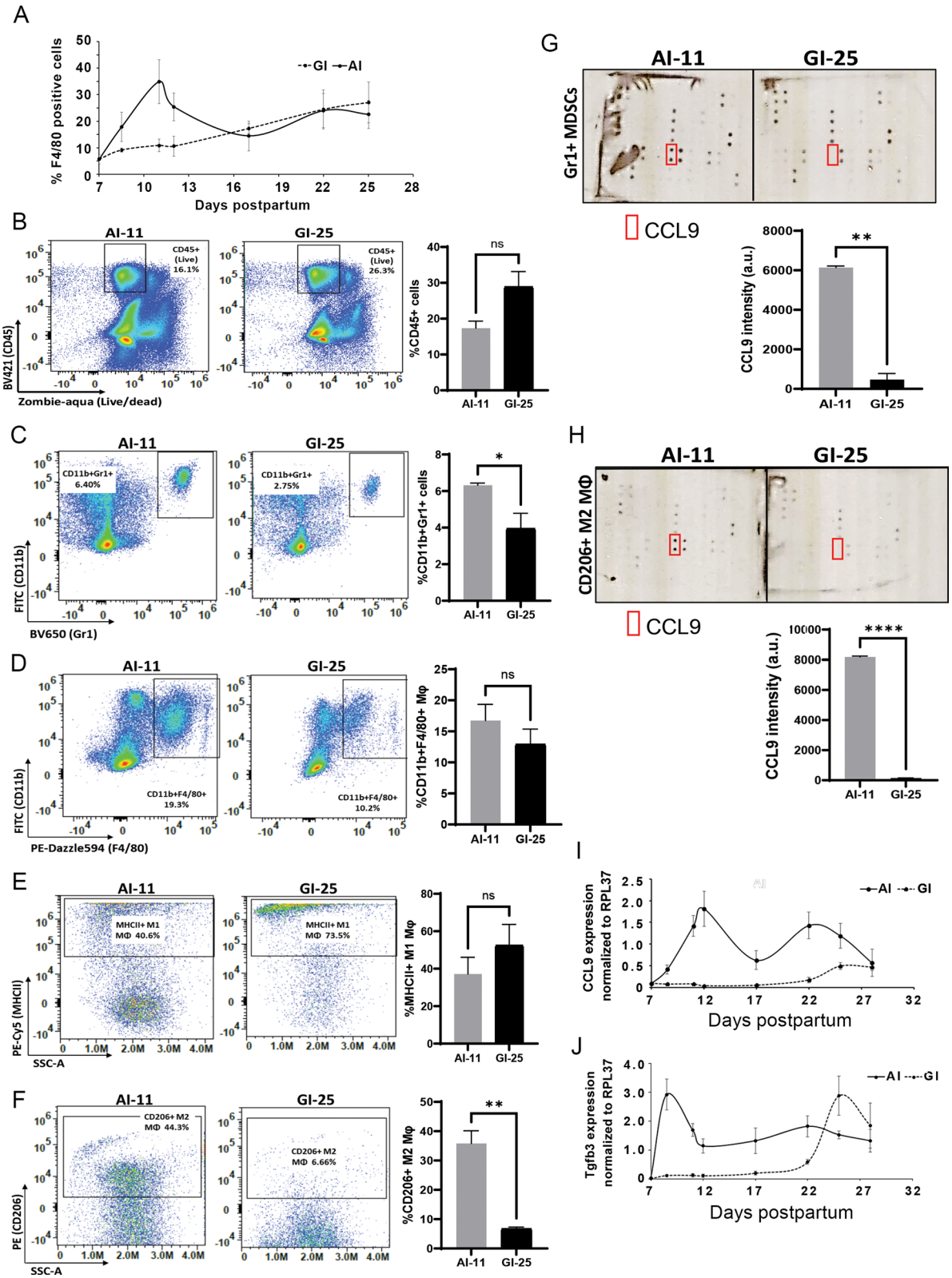

Fig. 4 (See legend on previous page.)

M2-like macrophages compared to GI glands, concomitant with elevated levels of CCL9 chemokine.

CCL9 promotes the expansion of ERα negative luminal progenitor cells

We previously reported the expansion of LP cell populations in AI but not GI mammary glands [13]. To further investigate the impact of CCL9 on LP cells, we cultured sorted LP cells from 6-week-old virgin female mice as 3D-organoids and treated them with mouse recombinant CCL9 (100 ng/mL). Three-dimensional organoids formed by different cell types recapitulate specific morphologies in vitro [40], and both mammary luminal and basal cells are maintained faithfully in 3D assays when cultured for a short time [41]. LP cells cultured on basal medium eagle (BME) without CCL9 treatment formed solid round organoids. In contrast, on day 12 of CCL9 treatment, we observed the formation of disorganized acinar-type organoids (Fig. 5A, panel 3), with a 6.6-fold increase in luminal budding and branching outgrowths (Fig. 5B, $p < 0.0001$). Interestingly, similar morphological differences were observed in LP cells isolated from AI and GI mammary glands on day 56 PPM and grown as organoids (Fig. 5C). A recent study demonstrated that basal/stem cells can form these disorganized organoids with luminal characteristics [40], suggesting that LP cells cultured in vitro may acquire basal phenotypes. To understand the effect of CCL9 on LP cells, we analyzed the expression of several genes associated with stemness (*CD133, CD49f, CD44*), proliferation (*Ki67*), basal *vs.* luminal characteristics (*Krt14, Krt8*), LP cell markers (*Elf5*) [42], and *Esr1*. Control organoids (untreated) and the organoids treated with CCL9 for 12 days as described previously (Fig. 5A) were used for RNA isolation and subjected to qRT-PCR. CCL9 treatment of the LP organoids for 12 days resulted in a significant increase in *Elf5* expression (twofold, $p = 0.004$), and a marked reduction in *Esr1* expression (−2.5-fold, $p = 0.001$) (Fig. 5D and E). Although there was

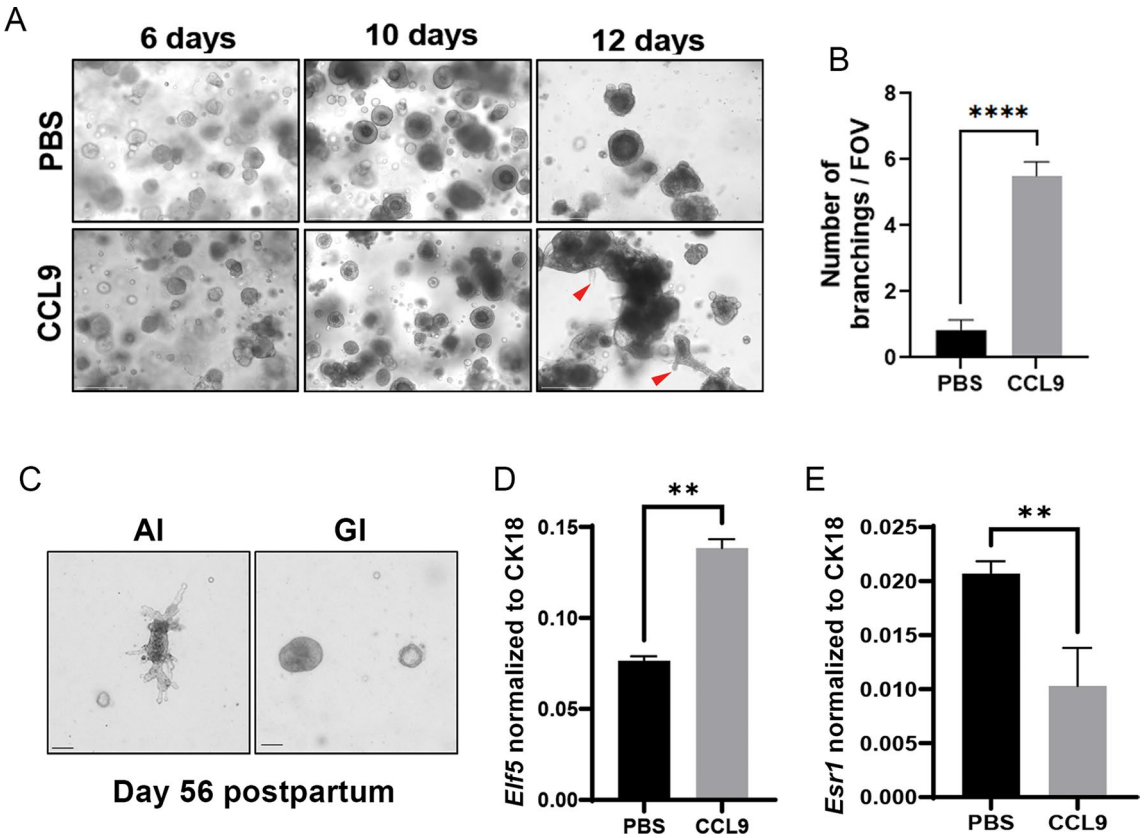

Fig. 5 CCL9 promotes the expansion of Elf5 positive/ERα negative luminal progenitor cells. **A.** Effect of murine CCL9 recombinant protein (100 ng/mL) on organoid culture of LP cells sorted from the mammary glands of 6-week-old female virgin mice treated for up to 12 days. PBS-treated organoids are referred to as control. Red arrowheads indicate filopodia-like structures. n = 3 per group. Scale bar: 275 µm. **B.** Quantification of luminal outgrowths (branching) in PBS *vs.* CCL9 treated LP cell-derived organoid on day12 of treatment. FOV: Field of view. Number of FOV = 6. **C.** LP cells isolated from AI and GI glands harvested on day 56 PPM are grown as organoids and imaged after 14 days in culture. n = 3 per group. Scale bar: 150 µm. **D.** Quantitative RT-PCR analysis of *Elf5* and **E.** *Esr1* expressions in organoids either treated with PBS or CCL9 protein for 12 days as described in Fig. 5A. *CK18* expression was used as normalizer. n = 3 per group. ns: non-significant, ***p*-value > 0.01

a trend toward increased *Ki67* expression after 12 days of CCL9 treatment (Supplementary Fig. S5A), no significant changes were observed in the expression of stem cell or basal markers (Supplementary Figs. S5A & S5C). Altogether, these findings suggest that CCL9 secreted by MDSCs and M2-like macrophages in AI glands during the peak of cell death leads to the expansion of ERα-negative LP cells, the putative cells of origin for basal-like breast cancer [14], without any discernable effect on their stemness.

Multiplexed high-dimensional imaging reveals substantial differences in CCL9-producing M2-like macrophages and ELF5 + LP cells in AI *vs.* GI glands

In this study, we utilized high-dimensional multiplexed imaging to comprehensively characterize the cellular dynamics in mammary glands with respect to AI *vs.* GI (Fig. 6A), focusing on the presence of specific cell types such as CCL9-producing CD206 + M2-like macrophages and ELF5 + LP cells expressing ERα and Wnt5a. Our approach also involved examining mammary glands harvested from various time points (Fig. 6A). Consistent with our flow cytometric findings, the multiplexed imaging confirmed a significantly increased abundance of CD206 + M2-like macrophages in AI-day 11 compared to GI-day 25 glands (Fig. 6B, Supplementary Fig. S6A). Additionally, we aimed to validate our cytokine/chemokine array results, which showed elevated expression of CCL9 by CD206 + M2-like macrophages. We observed a significant increase in CCL9 + CD206 + M2-like macrophages in AI-day 11 compared to GI-day 25 mammary glands (Fig. 6C, Supplementary Fig. S6B). Notably, there was no significant difference in the presence of CCR1 + (a well-defined receptor for CCL9) ELF5 + LP cells between these two groups (Supplementary Fig. S7A). Moreover, we observed a significantly higher number of ERα + ELF5 + LP cells in AI-day 11 compared to GI-day 25 mammary glands (Fig. 6D, Supplementary Fig. S6C).

We further compared the relative abundance of CD206 + M2-like macrophages in AI *vs.* GI on day 28 using multiplexed imaging, which revealed a significantly increased population of CD206 + M2-like macrophages in AI-day 28 mammary glands compared to GI-day 28 glands (Fig. 6E, Supplementary Fig. S6D). However, there were no significant differences in the abundance of CCL9-expressing CD206 + M2-like macrophages and CCR1 + ELF5 + LP cells between these two groups (Supplementary Figs. S7B & S7C). Remarkably, we observed a significantly higher level of WNT5a-expressing ELF5 + LP cells in AI-day 28 mammary glands compared to GI-day 28 (Fig. 6F, Supplementary Fig. S6E). This finding aligns with our previous results from GSEA of Affymetrix data, which indicated elevated expression of the *Wnt5a*, associated with the upregulated Notch and luminal progenitor pathways identified in AI mammary glands [13]. We have also noted a trend for higher ELF5 + cells in the AI-day 28 glands when compared to GI-day 28 glands but note that the difference as captured by multiplex IF was not significant (Fig. 6G, Supplementary Fig. S6F). Intriguingly, the percentage of ERα + ELF5 + cells is significantly lower in the AI glands as compared to the GI glands at this time point, suggesting a predominance of ERα- ELF5 + LP cells in the AI glands (Fig. 6H, Supplementary Fig. S6G). A significant increase in LP cell fraction has been reported in the preneoplastic lesions of *BRCA1* mutant carriers who are predisposed to basal-like breast cancer [14]. In our study, the significant increase in Elf5 + cells in AI glands demonstrates expansion of LP cell population compared to GI glands while ERα negativity of these cells signifies their potential to be precursors of basal-like breast cancer. Altogether, our multiplexed imaging of mammary glands harvested from AI *vs.* GI mice at different time points has revealed the differential abundance of CCL9-producing CD206 + M2-like macrophages and ELF5 + LP cells with diverse functional statuses.

In summary, our findings demonstrate that the duration of breastfeeding (short-term *vs.* prolonged) distinctly influences global remodeling of the post-lactational mammary gland environment. This impact extends beyond temporal considerations and includes quantitative and qualitative differences in apoptosis, inflammatory responses, myeloid cell infiltration, and expression patterns of genes related to DNA damage.

(See figure on next page.)

Fig. 6 Multiplex imaging demonstrates a distinct profile of epithelial and immune cells in AI *vs.* GI mammary glands. **A.** Schematic diagram showing the workflow of multiplexing imaging of selected markers in mammary glands of AI and GI mice at different time points. n = 3 per group and the number of fields analyzed is n = 12. **B-D.** The representative 10 × merged figures (inset 40 × merged) and bar diagrams showing the normalized % of **B.** CD206 + M2-like macrophages; **C.** CCL9 + CD206 + M2-like macrophages; and **D.** ERα expressing ELF5 + LP cells in mammary glands of AI-day 11 *vs.* GI-day 25 mice. **E–H.** The representative 10 × merged figures (inset 40 × merged) and bar diagrams showing the normalized **E.** % of CD206 + M2-like macrophages; **F.** Wnt5a + ELF5 + ; **G.** ELF5 + ; and **H.** ERα + ELF5 + LP cells in mammary glands of AI-day 28 *vs.* GI-day 28 mice. ns: non-significant, * p-value > 0.05, **p-value > 0.01, *** p-value > 0.001, **** *p*-value > 0.0001

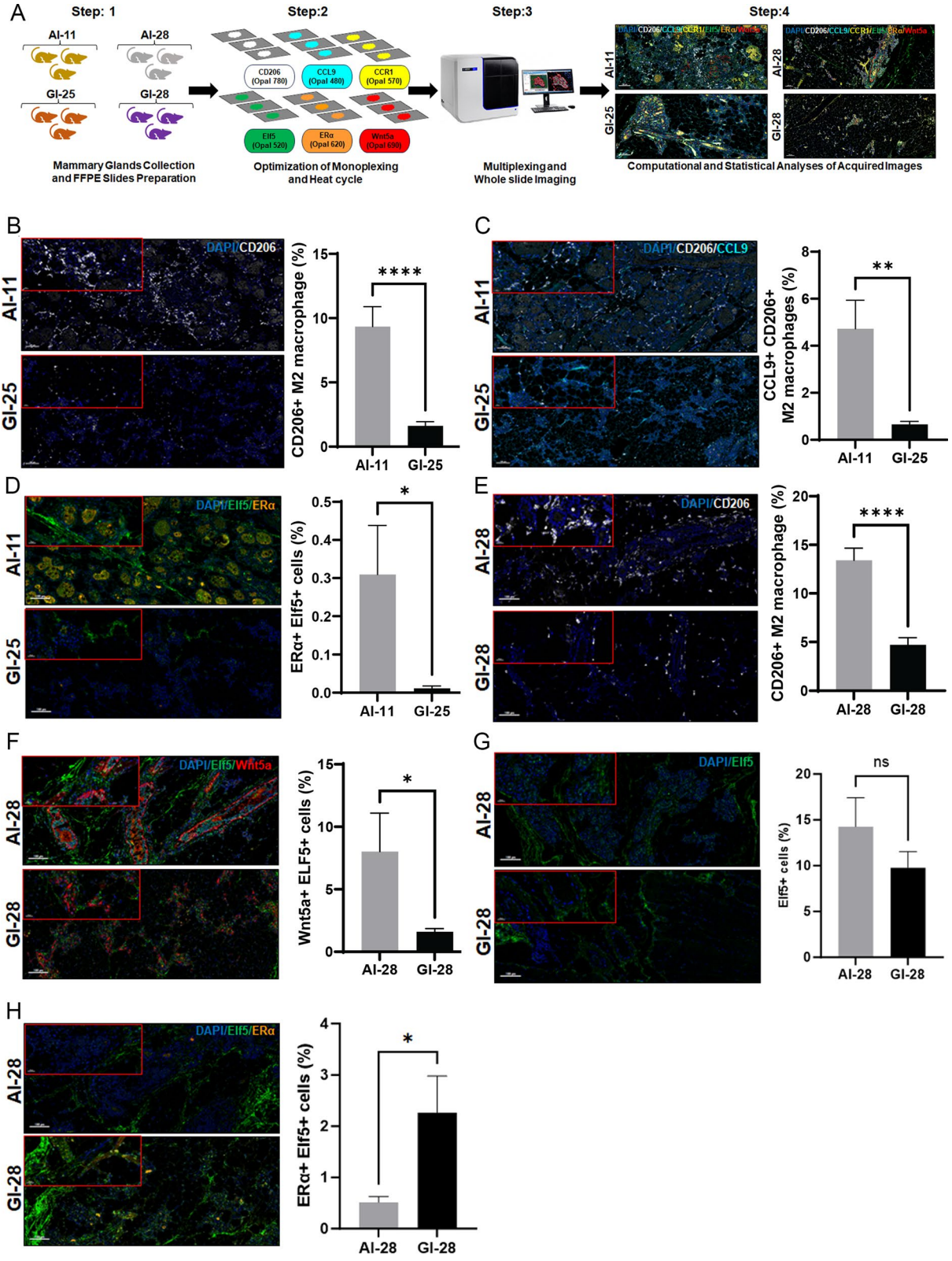

Fig. 6 (See legend on previous page.)

Discussion

Global population studies have shown that prolonged breastfeeding reduces the risk of developing breast cancer [9]. While reproductive risk factors are typically associated with modifying the chance of developing hormone receptor (HR)-positive breast cancer, growing literature demonstrates that higher parity coupled with lack of breastfeeding increases the risk of TNBC [1, 43, 44]. Despite the strong epidemiological data, the mechanistic relationship between breastfeeding and the risk of breast cancer, specifically TNBC, remains unclear. Therefore, understanding how GI, as opposed to AI, distinctly impacts mammary gland remodeling will not only delineate the biological link between breastfeeding and breast cancer risk, but will help in identifying prevention strategies for high-risk women who cannot breastfeed. Our previous work using mouse models of involution showed a persistent and long-term effect of AI, but not GI, that led to an increase in inflammation and collagen deposition and resulted in alveolar hyperplasia [13]. Our current study demonstrates that the physiological response at the early stage of mammary gland involution depends on breastfeeding duration, shedding insight into how this modifies breast cancer risk. Schematics highlighting the factors studied in the context of AI *vs.* GI and our key findings are presented in Fig. 7A & B.

Involution is a multi-step process initiated by weaning and milk stasis with an increase in pro-apoptotic factors and clearance of mammary epithelial cells (MEC) [23]. It is reversible within 48 h if suckling is reinitiated, and this process is largely regulated by Rac1 in mice [45]. This is followed by an irreversible process of ongoing apoptosis and tissue remodeling. Much of our understanding of these processes is from animal studies using forced weaning protocols at days 7–10 PPM resulting in abruptly involuted mammary glands [27, 29, 46]. Our study highlights the differences in intensity and duration of this massive remodeling between AI and GI glands where cell death kinetics is distinct and adipocyte repopulation in GI glands occurs rather acutely as opposed to a rather gradual process in AI glands. Zwik et al. reported that hypertrophy of mature adipocytes and not adipogenesis is the primary mechanism of adipocyte repopulation during AI of mouse mammary glands [47]. The precise mechanism of adipocyte repopulation during GI is beyond the scope of this study, though it is a worthy topic for further investigation.

Using an AI model, Wärri et al. reported an interplay of autophagy, unfolded protein response, and apoptosis that regulates involution [20], where in C57BL/6 mice, the BCL-xL level peaked 24 h post AI followed by a gradual decrease over 72 h. In these mice, the cleaved PARP (89 kDa) level peaked between 48 and 72 h of inducing AI, followed by a sharp decline. In our studies with FVB/N female mice, BCL-xL showed a bimodal pattern of expression in AI glands with the first increase coinciding with cell death peak and a second peak at day 28 PPM. Given that a high BCL-xL level is favorable for proliferation and growth [48], it can be speculated that the increase in BCL-xL at the later time point is supportive of epithelial cell growth. Intriguingly, in the FVB/N mice, the 89 kDa cleaved PARP, a product of caspase-mediated cleavage, was not detectable either in AI or GI glands. On the contrary, a 55 kDa and a 24 kDa cleaved PARP fragments were predominant in both GI and AI glands, products of cathepsin-mediated PARP cleavage [25, 26]. Major involvement of cathepsin B and L in lysosome-mediated programmed cell death during AI of mammary glands was previously described [27] and supports our data. Interestingly, the 24 kDa PARP fragment, a trans-dominant inhibitor of active PARP, had late and relatively sustained elevated levels in GI glands, in contrast to AI glands. This could lead to overactivation of PARP in the AI glands, blocking cell death and allowing damaged cells to propagate unlike in GI glands. The subtle differences observed during cell death in AI glands could be due to differences in mouse strains and are worthy of further study.

There were some distinct differences in the expression of acute phase response (APR) genes in AI *vs.* GI glands (summarized in Table 1), suggesting differing mechanisms underlying the two modes of involution. While increase in pStat3 is obvious in both AI and GI mammary glands, the downstream effector *C/EBPδ* [30] was not detectable in GI glands. C/EBPδ that promotes epithelial cell death during mammary gland involution, is a mediator of inflammatory cytokine signaling and is considered to promote pro-tumorigenic environment [49]. However, its role in breast carcinogenesis is unclear. Similarly, *CtsL* is exclusively detected in AI glands. High levels of CTSL have been directly correlated with shorter recurrence free, overall and distant metastasis free survival in TNBC patients [50]. The most insightful of all is the noticeably high expression of *Slpi* and *CD14* in the AI glands. Slpi protects tissue from proteases such as cathepsin D [31] and higher *Slpi* expression is correlated with worse outcome in TNBC patients [51]. Significantly elevated level of *Slpi* in AI glands implies a high degree of tissue injury during AI and an attempt to protect the glands. CD14, shown to be expressed by mammary epithelial cells and participating in dead cell clearance [19], was differentially elevated in AI glands further contrasting AI from GI process. With respect to Chi3L1, a mammalian glycoprotein increased in inflammatory conditions and cancer [52], our results are in line with previous reports demonstrating heightened levels in the AI glands [30]. *Chi3L*

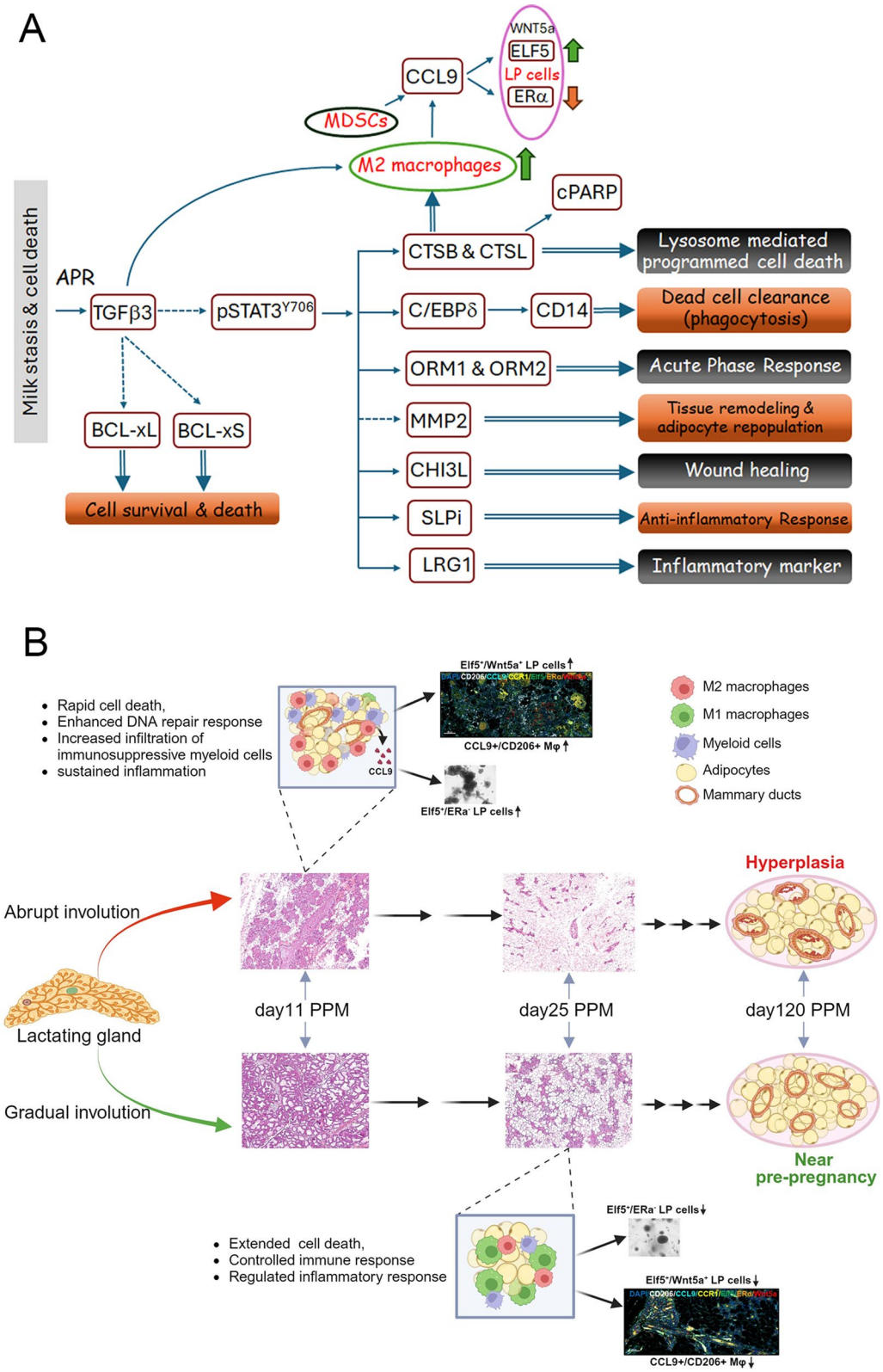

Fig. 7 **A.** Key factors involved in differential regulation of abrupt involution in mouse mammary gland and its long-term impact. Milk stasis and massive cell death during AI triggers Acute phase response (APR) and cascade of events regulated predominantly by TGFβ3 and STAT3 directly (solid arrows) or indirectly (broken arrows). **B.** Schematic summarizing the early events during abrupt *vs.* gradual involution leading to precancerous changes in the AI gland as opposed to remodeling to near pre-pregnancy state in the GI glands

expression is sustained over a longer period of time, suggesting extended inflammatory state in AI glands in contrast with GI glands. Analysis of APR genes clearly demonstrated a distinct pattern of involution in AI *vs.* GI mammary glands in mice that could contribute to increased breast cancer risk following lack of or short-term breastfeeding.

Immune cells are key players during involution, clearing the dead cells and aiding in global remodeling of the lactating glands. A previous study reported a high density of leukocytes (CD45+) on day 3 of abrupt involution, which quickly declined on day 6 [46]. We observed a similar trend in leukocytes and macrophages (CD11b+F4/80+) in the AI gland and GI glands at the peak of cell deaths. Interestingly, while there was significant enrichment of M2-like macrophages in the AI glands, it was less in the GI glands by ~ 80%. Schedin's lab has elegantly demonstrated the critical role of M2-like macrophages during mammary gland involution, specifically in the AI setting, where milk stasis and *Stat3* activation alone fail to execute involution [46]. Intriguingly, CCL9 expression by the M2 macrophages and MDSCs exclusively in the involuting AI glands, raises the possibility of CCL9 being a master regulator of events distinguishing AI from GI. This is particularly important in the context of the expansion of ELF5+ERα- cells when LP spheroids were exposed to CCL9. Intriguingly, we have reported the expansion of LP cells in AI glands previously [13], and Lim et al. determined ERα- LP cells to be the putative precursors of TNBC [14]. Future cell lineage tracing studies could determine if these specific cells are precursors of precancerous lesions in abruptly involuting glands [13].

Our high-dimensional multiplex IF on mammary sections showing significantly higher populations of CD206+M2-like macrophages and an elevated level of Wnt5a-expressing ELF5+LP cells in fully involuted AI glands, corroborates our earlier data of higher abundance of macrophages in involuted AI glands, and enrichment of Notch signaling pathway in LP cells from AI, but not GI glands. Importantly, the AI glands at peak of involution are enriched for CCL9+/CD206+cells. This is certainly unique to AI glands and our study highlights a novel function of CCL9 in expansion of ERα-/ELF5 + LP cells. Importantly, there are two discrete populations of LP cells in the mammary gland: a major ERα- population and a smaller ERα+population. Visvader's lab previously showed that while the human breast has ~ 25% ERα+luminal restricted cells, the mouse mammary gland has only ~ 5% [53]. Our study reveals similar findings where only ~ 3% of the ELF5+cells are ERα positive in the GI gland. This provides additional evidence that our murine model is a valuable animal model to study breast involution. Interestingly, reduced ELF5+/ERα+cell population in spite of higher ELF5+cells in the AI gland, indicates predominance of ERα-/ ELF5+cells in the AI-day 28 glands, supporting our in vitro data and highlighting the distinct molecular events underlying AI *vs.* GI. Our findings collectively relate AI to increased breast cancer risk and highlight the fact that early events during mammary gland involution could have a profound impact on future breast cancer risk.

Multiple studies have shown how full-term pregnancy alters the mammary glands when compared to the nulliparous gland and protects against carcinogenic insult [54]. On the other hand, pregnancy places a mother at a higher risk for aggressive pregnancy-associated breast cancer, and our observations indicate long-term breastfeeding could alter or reduce this risk [55]. In addition, one major biological contributing factor to higher mortality in African American women is the higher incidence of the more aggressive TNBC [56–58]. The African American Breast Cancer Epidemiology and Risk (AMBER) Consortium report associates ever-breastfeeding with a reduced risk of HR-negative breast cancer and states that prolonged breastfeeding could further ameliorate this risk [11]. The Carolina Breast Cancer Study reported that longer-duration breastfeeding was associated with a reduced risk of TNBC in Black women [56]. The prevalence of breastfeeding has been historically low among Black women [43]. While addressing racial disparity in cancer outcomes should include addressing barriers to breastfeeding in Black women, a mechanistic understanding of differences between the effect of prolonged *vs.* a lack of or short-term breastfeeding addressed in this study will lead to options for preventive measures.

While our work has shown a distinct impact of AI *vs.* GI in mouse mammary glands, increasing the risk of breast cancer with further hits, the lack of a breast cancer model that shows development of invasive cancer just by altering the process of involution is a limitation.

Conclusions and significance

Our preclinical mouse model of GI *vs.* AI shows that AI triggers rapid cell death leading to heightened inflammation and promoting infiltration of myeloid cells. On the contrary, GI induces a controlled immune response resulting from prolonged cell death, facilitating comprehensive mammary gland remodeling. CCL9 secreted by myeloid cells in the AI glands but not in GI glands promotes the expansion of ERα negative luminal progenitor cells, the putative cells of origin of TNBC, thus connecting early events during AI to increased risk of breast cancer. From the public health perspective this work is highly significant and impactful. Understanding the mechanisms will increase prevention strategies even

for those mothers who cannot breastfeed and empowering all mothers and providers with this knowledge of risk reduction will improve the uptake of breastfeeding practices and improve racial disparities in breast cancer mortality.

Supplementary Information

The online version contains supplementary material available at https://doi.org/10.1186/s13058-024-01933-3.

Additional file 1.

Additional file 2.

Acknowledgements
We thank Angela Dahlberg of Ohio State University for her editorial help and Dr. Annapurna Gupta for technical help.

Author contributions
Conceptualization: S. Ma. and B.R.; Methodology: S. Ma., B.R., S. Mi., N.S., K.O, A.E.V.; Investigation: S. Mi., N.S., M.B., K.O., M.M.B., S.A., R.M., V.B., D.A., G.S.; Formal Analysis: S. Ma, X. Z., S. Mi., N.S., K.O.; Writing-original draft: S. Ma., S. Mi.; Writing-Reviewing & Editing: B.R., R.G., X.Z.; Funding Acquisition: B.R, R.G., A.E.V.; Supervision: S. Ma., B.R., R.G.

Funding
This research is supported by NIH R01 (CA231857) to B.R & R.K.G., NIH R01 (CA292020) and Department of Defense Breast Cancer Breakthrough (W81XWH1910088) awards to R.K.G., NIH R37 (CA233770-01) to A.E.V., and Department of Defense grant (W81XWH2210019) to A.E.V. Research reported in this publication was supported by The Ohio State University Comprehensive Cancer Center and the National Institutes of Health under grant number P30 CA016058 (OSUCCC Genomics core facility, Flow cytometry core facility).

Availability of data and materials
No datasets were generated or analysed during the current study.

Declarations

Ethics approval and consent to participate
All animal studies were performed according to the Institutional Animal Care and Use Committee of the Ohio State University guidelines.

Competing Interests
The authors declare no competing interests.

Author details
[1]Division of Medical Oncology, The Ohio State University Comprehensive Cancer Center, Columbus, OH, USA. [2]Department of Pathology, The Ohio State University, Columbus, OH 43210, USA. [3]Department of Radiation Oncology, The Ohio State University, Columbus, OH, USA. [4]Department of Biomedical Informatics and Center for Biostatistics, The Ohio State University, Columbus, OH, USA.

Received: 9 May 2024 Accepted: 21 November 2024
Published online: 03 January 2025

References

1. Ambrosone CB, Zirpoli G, Ruszczyk M, Shankar J, Hong CC, McIlwain D, Roberts M, Yao S, McCann SE, Ciupak G, et al. Parity and breastfeeding among African-American women: differential effects on breast cancer risk by estrogen receptor status in the Women's Circle of Health Study. Cancer Causes Control. 2014;25(2):259–65.
2. Warner ET, Tamimi RM, Boggs DA, Rosner B, Rosenberg L, Colditz GA, Palmer JR. Estrogen receptor positive tumors: do reproductive factors explain differences in incidence between black and white women? Cancer Causes Control. 2013;24(4):731–9.
3. Society. AC: Breast Cancer Facts & Figures 2022–2024. Atlanta: American Cancer Society, Inc 2022
4. Sturtz LA, Melley J, Mamula K, Shriver CD, Ellsworth RE. Outcome disparities in African American women with triple negative breast cancer: a comparison of epidemiological and molecular factors between African American and Caucasian women with triple negative breast cancer. BMC Cancer. 2014;14:62.
5. Macias H, Hinck L. Mammary gland development. Wiley Interdiscip Rev Dev Biol. 2012;1(4):533–57.
6. Lund LR, Romer J, Thomasset N, Solberg H, Pyke C, Bissell MJ, Dano K, Werb Z. Two distinct phases of apoptosis in mammary gland involution: proteinase-independent and -dependent pathways. Development. 1996;122(1):181–93.
7. Balogh GA, Heulings R, Mailo DA, Russo PA, Sheriff F, Russo IH, Moral R, Russo J. Genomic signature induced by pregnancy in the human breast. Int J Oncol. 2006;28(2):399–410.
8. D'Cruz CM, Moody SE, Master SR, Hartman JL, Keiper EA, Imielinski MB, Cox JD, Wang JY, Ha SI, Keister BA, et al. Persistent parity-induced changes in growth factors, TGF-beta3, and differentiation in the rodent mammary gland. Mol Endocrinol. 2002;16(9):2034–51.
9. Breast cancer and breastfeeding. collaborative reanalysis of individual data from 47 epidemiological studies in 30 countries, including 50302 women with breast cancer and 96973 women without the disease. Lancet. 2002;360(9328):187–95.
10. Palmer JR, Ambrosone CB, Olshan AF. A collaborative study of the etiology of breast cancer subtypes in African American women: the AMBER consortium. Cancer Causes Control. 2014;25(3):309–19.
11. Palmer JR, Viscidi E, Troester MA, Hong CC, Schedin P, Bethea TN, Bandera EV, Borges V, McKinnon C, Haiman CA, et al. Parity, lactation, and breast cancer subtypes in African American women: results from the AMBER Consortium. J Nat Cancer Inst. 2014. https://doi.org/10.1093/jnci/dju237.
12. Phipps AI, Chlebowski RT, Prentice R, McTiernan A, Wactawski-Wende J, Kuller LH, Adams-Campbell LL, Lane D, Stefanick ML, Vitolins M, et al. Reproductive history and oral contraceptive use in relation to risk of triple-negative breast cancer. J Natl Cancer Inst. 2011;103(6):470–7.
13. Basree MM, Shinde N, Koivisto C, Cuitino M, Kladney R, Zhang J, Stephens J, Palettas M, Zhang A, Kim HK, et al. Abrupt involution induces inflammation, estrogenic signaling, and hyperplasia linking lack of breastfeeding with increased risk of breast cancer. Breast cancer research : BCR. 2019;21(1):80.
14. Lim E, Vaillant F, Wu D, Forrest NC, Pal B, Hart AH, Asselin-Labat ML, Gyorki DE, Ward T, Partanen A, et al. Aberrant luminal progenitors as the candidate target population for basal tumor development in BRCA1 mutation carriers. Nat Med. 2009;15(8):907–13.
15. Mishra S, Charan M, Shukla RK, Agarwal P, Misri S, Verma AK, Ahirwar DK, Siddiqui J, Kaul K, Sahu N, et al. cPLA2 blockade attenuates S100A7-mediated breast tumorigenicity by inhibiting the immunosuppressive tumor microenvironment. J Exp Clin Cancer Res. 2022;41(1):54.
16. Vilgelm AE, Bergdorf K, Wolf M, Bharti V, Shattuck-Brandt R, Blevins A, Jones C, Phifer C, Lee M, Lowe C, et al. Fine-needle aspiration-based patient-derived cancer organoids. iScience. 2020;23(8): 101408.
17. Bharti V, Watkins R, Kumar A, Shattuck-Brandt RL, Mossing A, Mittra A, Shen C, Tsung A, Davies AE, Hanel W, et al. BCL-xL inhibition potentiates cancer therapies by redirecting the outcome of p53 activation from senescence to apoptosis. Cell Rep. 2022;41(12): 111826.
18. Hughes K, Wickenden JA, Allen JE, Watson CJ. Conditional deletion of Stat3 in mammary epithelium impairs the acute phase response and modulates immune cell numbers during post-lactational regression. J Pathol. 2012;227(1):106–17.
19. Stein T, Morris JS, Davies CR, Weber-Hall SJ, Duffy MA, Heath VJ, Bell AK, Ferrier RK, Sandilands GP, Gusterson BA. Involution of the mouse mammary gland is associated with an immune cascade and an acute-phase response, involving LBP, CD14 and STAT3. Breast cancer research : BCR. 2004;6(2):R75-91.
20. Warri A, Cook KL, Hu R, Jin L, Zwart A, Soto-Pantoja DR, Liu J, Finkel T, Clarke R. Autophagy and unfolded protein response (UPR) regulate mammary gland involution by restraining apoptosis-driven irreversible changes. Cell Death Discov. 2018;4:40.

21. Liberzon A, Birger C, Thorvaldsdottir H, Ghandi M, Mesirov JP, Tamayo P. The molecular signatures database (MSigDB) hallmark gene set collection. Cell Syst. 2015;1(6):417–25.
22. Chang CH, Zhang M, Rajapakshe K, Coarfa C, Edwards D, Huang S, Rosen JM. Mammary stem cells and tumor-initiating cells are more resistant to apoptosis and exhibit increased DNA repair activity in response to DNA damage. Stem Cell Reports. 2015;5(3):378–91.
23. Watson CJ. Involution: apoptosis and tissue remodelling that convert the mammary gland from milk factory to a quiescent organ. Breast Cancer Research : BCR. 2006;8(2):203.
24. Heermeier K, Benedict M, Li M, Furth P, Nunez G, Hennighausen L. Bax and Bcl-xs are induced at the onset of apoptosis in involuting mammary epithelial cells. Mech Dev. 1996;56(1–2):197–207.
25. Gobeil S, Boucher CC, Nadeau D, Poirier GG. Characterization of the necrotic cleavage of poly(ADP-ribose) polymerase (PARP-1): implication of lysosomal proteases. Cell Death Differ. 2001;8(6):588–94.
26. Chaitanya GV, Steven AJ, Babu PP. PARP-1 cleavage fragments: signatures of cell-death proteases in neurodegeneration. Cell Commun Signal. 2010;8:31.
27. Kreuzaler PA, Staniszewska AD, Li W, Omidvar N, Kedjouar B, Turkson J, Poli V, Flavell RA, Clarkson RW, Watson CJ. Stat3 controls lysosomal-mediated cell death in vivo. Nat Cell Biol. 2011;13(3):303–9.
28. Clarkson RW, Wayland MT, Lee J, Freeman T, Watson CJ. Gene expression profiling of mammary gland development reveals putative roles for death receptors and immune mediators in post-lactational regression. Breast cancer research : BCR. 2004;6(2):R92-109.
29. Sargeant TJ, Lloyd-Lewis B, Resemann HK, Ramos-Montoya A, Skepper J, Watson CJ. Stat3 controls cell death during mammary gland involution by regulating uptake of milk fat globules and lysosomal membrane permeabilization. Nat Cell Biol. 2014;16(11):1057–68.
30. Thangaraju M, Rudelius M, Bierie B, Raffeld M, Sharan S, Hennighausen L, Huang AM, Sterneck E. C/EBPdelta is a crucial regulator of pro-apoptotic gene expression during mammary gland involution. Development. 2005;132(21):4675–85.
31. Doumas S, Kolokotronis A, Stefanopoulos P. Anti-inflammatory and antimicrobial roles of secretory leukocyte protease inhibitor. Infect Immun. 2005;73(3):1271–4.
32. Scully S, Yan W, Bentley B, Cao QJ, Shao R. Inhibitory activity of YKL-40 in mammary epithelial cell differentiation and polarization induced by lactogenic hormones: a role in mammary tissue involution. PLoS ONE. 2011;6(10): e25819.
33. Uria JA, Werb Z. Matrix metalloproteinases and their expression in mammary gland. Cell Res. 1998;8(3):187–94.
34. Wilson GJ, Fukuoka A, Vidler F, Graham GJ. Diverse myeloid cells are recruited to the developing and inflamed mammary gland. Immunology. 2022;165(2):206–18.
35. Hitchcock J, Hughes K, Pensa S, Lloyd-Lewis B, Watson CJ. The immune environment of the mammary gland fluctuates during post-lactational regression and correlates with tumour growth rate. Development. 2022;149(8):dev200162.
36. Ahirwar DK, Charan M, Mishra S, Verma AK, Shilo K, Ramaswamy B, Ganju RK. Slit2 inhibits breast cancer metastasis by activating M1-like phagocytic and antifibrotic macrophages. Can Res. 2021;81(20):5255–67.
37. Yan HH, Jiang J, Pang Y, Achyut BR, Lizardo M, Liang X, Hunter K, Khanna C, Hollander C, Yang L. CCL9 Induced by TGFbeta signaling in myeloid cells enhances tumor cell survival in the premetastatic organ. Can Res. 2015;75(24):5283–98.
38. Guo Q, Betts C, Pennock N, Mitchell E, Schedin P. Mammary gland involution provides a unique model to study the TGF-beta cancer paradox. J Clin Med. 2017;6(1):10.
39. Nguyen AV, Pollard JW. Transforming growth factor beta3 induces cell death during the first stage of mammary gland involution. Development. 2000;127(14):3107–18.
40. Rosenbluth JM, Schackmann RCJ, Gray GK, Selfors LM, Li CM, Boedicker M, Kuiken HJ, Richardson A, Brock J, Garber J, et al. Organoid cultures from normal and cancer-prone human breast tissues preserve complex epithelial lineages. Nat Commun. 2020;11(1):1711.
41. Shackleton M, Vaillant F, Simpson KJ, Stingl J, Smyth GK, Asselin-Labat ML, Wu L, Lindeman GJ, Visvader JE. Generation of a functional mammary gland from a single stem cell. Nature. 2006;439(7072):84–8.
42. Oakes SR, Naylor MJ, Asselin-Labat ML, Blazek KD, Gardiner-Garden M, Hilton HN, Kazlauskas M, Pritchard MA, Chodosh LA, Pfeffer PL, et al. The Ets transcription factor Elf5 specifies mammary alveolar cell fate. Genes Dev. 2008;22(5):581–6.
43 Anstey EH, Shoemaker ML, Barrera CM, O'Neil ME, Verma AB, Holman DM. Breastfeeding and Breast Cancer Risk Reduction: Implications for Black Mothers. Am J Prev Med. 2017;53(3s1):s40–6.
44. John EM, Hines LM, Phipps AI, Koo J, Longacre TA, Ingles SA, Baumgartner KB, Slattery ML, Wu AH. Reproductive history, breast-feeding and risk of triple negative breast cancer: the Breast Cancer Etiology in Minorities (BEM) study. Int J Cancer. 2018;142(11):2273–85.
45. Mironov A, Fisher M, Narayanan P, Elsayed R, Karabulutoglu M, Akhtar N. Rac1 controls cell turnover and reversibility of the involution process in postpartum mammary glands. PLoS Biol. 2023;21(1): e3001583.
46. O'Brien J, Martinson H, Durand-Rougely C, Schedin P. Macrophages are crucial for epithelial cell death and adipocyte repopulation during mammary gland involution. Development. 2012;139(2):269–75.
47. Zwick RK, Rudolph MC, Shook BA, Holtrup B, Roth E, Lei V, Van Keymeulen A, Seewaldt V, Kwei S, Wysolmerski J, et al. Adipocyte hypertrophy and lipid dynamics underlie mammary gland remodeling after lactation. Nat Commun. 2018;9(1):3592.
48. Hartman ML, Czyz M. BCL-w: apoptotic and non-apoptotic role in health and disease. Cell Death Dis. 2020;11(4):260.
49. Hartl L, Duitman J, Bijlsma MF, Spek CA. The dual role of C/EBPdelta in cancer. Crit Rev Oncol Hematol. 2023;185: 103983.
50. Zhang L, Zhao Y, Yang J, Zhu Y, Li T, Liu X, Zhang P, Cheng J, Sun S, Wei C, et al. CTSL, a prognostic marker of breast cancer, that promotes proliferation, migration, and invasion in cells in triple-negative breast cancer. Front Oncol. 2023;13:1158087.
51. Kozin SV, Maimon N, Wang R, Gupta N, Munn L, Jain RK, Garkavtsev I. Secretory leukocyte protease inhibitor (SLPI) as a potential target for inhibiting metastasis of triple-negative breast cancers. Oncotarget. 2017;8(65):108292–302.
52. Libreros S, Garcia-Areas R, Iragavarapu-Charyulu V. CHI3L1 plays a role in cancer through enhanced production of pro-inflammatory/pro-tumorigenic and angiogenic factors. Immunol Res. 2013;57(1–3):99–105.
53. Fu NY, Nolan E, Lindeman GJ, Visvader JE. Stem Cells and the Differentiation Hierarchy in Mammary Gland Development. Physiol Rev. 2020;100(2):489–523.
54. Russo J, Moral R, Balogh GA, Mailo D, Russo IH. The protective role of pregnancy in breast cancer. Breast cancer research : BCR. 2005;7(3):131–42.
55 Galati F, Magri V, Arias-Cadena PA, Moffa G, Rizzo V, Pasculli M, Botticelli A, Pediconi F. Pregnancy-associated breast cancer: a diagnostic and therapeutic challenge. Diagnostics (Basel). 2023;13(4):604.
56. Carey LA, Perou CM, Livasy CA, Dressler LG, Cowan D, Conway K, Karaca G, Troester MA, Tse CK, Edmiston S, et al. Race, breast cancer subtypes, and survival in the Carolina Breast Cancer Study. JAMA. 2006;295(21):2492–502.
57. Bauer KR, Brown M, Cress RD, Parise CA, Caggiano V. Descriptive analysis of estrogen receptor (ER)-negative, progesterone receptor (PR)-negative, and HER2-negative invasive breast cancer, the so-called triple-negative phenotype: a population-based study from the California cancer Registry. Cancer. 2007;109(9):1721–8.
58. Morris GJ, Naidu S, Topham AK, Guiles F, Xu Y, McCue P, Schwartz GF, Park PK, Rosenberg AL, Brill K, et al. Differences in breast carcinoma characteristics in newly diagnosed African-American and Caucasian patients: a single-institution compilation compared with the National Cancer Institute's Surveillance, Epidemiology, and End Results database. Cancer. 2007;110(4):876–84.

Publisher's Note